PHYSICAL REVIEW D VOLUME 38, NUMBER 7 1 OCTOBER 1988

Neutrino production by 400-GeV/c protons in a beam-dump experiment

M. E. Duffy,[a] G. K. Fanourakis,[b] R. J. Loveless, D. D. Reeder, and E. S. Smith[c]
University of Wisconsin, Madison, Wisconsin 53706

S. Childress
Fermilab, Batavia, Illinois 60510

C. Castoldi[d] and G. Conforto
Istituto Nazionale di Fisica Nucleare, Firenze, Italy

R. C. Ball, C. T. Coffin, H. R. Gustafson, L. W. Jones, I. D. Leedom,[e] M. J. Longo, T. J. Roberts,[f] B. P. Roe, and E. Wang[g]
University of Michigan, Ann Arbor, Michigan 48109

M. B. Crisler,[h] J. S. Hoftun,[i] T. Y. Ling, T. A. Romanowski, and J. T. Volk[j]
Ohio State University, Columbus, Ohio 43210

(Received 4 February 1988)

The ν_e and ν_μ fluxes from decay of short-lived parents (presumed to be predominantly charmed particles) have been measured in a beam-dump experiment at Fermilab. Novel and important features of the experimental arrangement and procedures are presented and discussed in detail. Details of the analysis of the prompt flux and the backgrounds are presented together with a discussion of the systematic error. The energy and angular distributions of the prompt neutrino flux are presented, and the cross section for charm production is measured to be $57.2\pm2.9\pm8.5$ μb/nucleon. The dependence of the cross section on atomic weight is measured to be $\sigma_c \propto A^{0.75}$. The possibility that charm is produced by a mixture of central and diffractive processes is examined and discussed in the context of these results. The prompt fluxes of ν_μ and $\bar{\nu}_\mu$ are roughly equal, as are the prompt fluxes of ν_μ and ν_e. Quasielastic neutrino interactions were identified and used to provide an independent measurement of the flux which corroborates the energy calibration of the detector. A search for additional sources of prompt neutrinos beyond charm is reported. Negative results were obtained for supersymmetric particles, heavy neutral leptons, and b quarks, subject to the assumption of specific characteristics of the particles and the production mechanisms.

I. INTRODUCTION

In the early 1970s, amid the confusing clutter of weakly decaying particles (lifetime $\tau \sim 10^{-10}$ sec) and resonances ($\tau \sim 10^{-23}$ sec), it was realized that contemporary experiments were incapable of detecting new particles whose lifetime was several orders of magnitude ($\sim 10^{-13}$ sec) less than that of strange particles. To search for such particles it was proposed to "dump" the proton beam into a large target, such that all the hadrons and muons produced in the interaction would be either absorbed or deflected. Neutrinos would survive to be detected downstream. The semileptonic decay of new, short-lived particles would produce "prompt" neutrinos, which could be distinguished from the "nonprompt" ν and $\bar{\nu}$ which come from the ordinary weak decays of π and K mesons.

Indeed, the early indications[1] of the production of new particles in neutrino interactions were based in part on comparison of dimuon production in targets of different density, a technique pioneered by Adair.[2] After the discovery of the J/ψ (closed charm) in 1974 (Refs. 3 and 4) and open charm in 1976 (Ref. 5), a beam-dump experiment was done at CERN using a copper target with three independent detectors: by the CERN-Dortmund-Heidelberg-Saclay[6] (CDHS) Collaboration; by the CERN-Hamburg-Amsterdam-Rome-Moscow[7] (CHARM) Collaboration; and by the Big European Bubble Chamber[8] (BEBC) Collaboration. In addition to searching for the presence of charm, these experiments were also looking for other new short-lived particles. Although the standard model of weak interactions predicts a prompt neutrino flux for which $\nu_e \simeq \nu_\mu$, these early experiments found $\nu_e/\nu_\mu = 0.48\pm0.12\pm0.10$ (CHARM), $\nu_e/\nu_\mu = 0.59^{+0.35}_{-0.21}$ (BEBC), and $\nu_e/\nu_\mu = 0.64^{+0.22}_{-0.15}$ (CDHS). These results were inconsistent with theoretical dogma and were widely interpreted as suggestive of new particles or processes.[9]

In the second-generation beam-dump experiment described here, the goal was to confirm (or refute) these results and to extend them. The important features of the experimental design were (1) the minimization of sources of false prompt neutrinos; (2) an alternative method for the identification of ν_e charged-current (CC) events using longitudinal shower development; (3) a large angular acceptance (≥ 30 mrad), which was made possible in part by using active magnetic shielding to shorten the distance between target and detector; and (4) the use of several targets to measure *A* dependence of charm production.

In addition to determining the details of hadronic charm production,[10] these design features also permit a search for other new phenomena: *b*-quark production, supersymmetric particles, and new heavy leptons. Such searches utilize the large angular acceptance of the neutrino detector (useful in detecting large $p_\perp$ decays) and the identification in the calorimeter of showers composed only of electrons and photons.

II. EXPERIMENTAL APPARATUS

A. Beam line

It is crucial to the beam-dump concept that the proton beam be carefully collimated upstream of the dump target. Interactions of protons with components of the beam transport system produce π and K mesons which decay to neutrinos. Since this flux of neutrinos is independent of target density, it would be attributed to "prompt" neutrinos and, thus, to charm production. Since the upstream background would consist predominantly of ν_μ, the measurement of prompt ν_e/ν_μ would be directly affected. In fact, suspicion of the early CERN beam-dump results, which found $\nu_e/\nu_\mu \sim 0.6$, centered on the possibility that some neutrinos were produced upstream of the target. We note, however, that subsequent tests and measurements provided no evidence for such upstream background.[11]

The proton beam in this experiment was transported by the *M*2 beam line in the Meson Laboratory of the Fermi National Accelerator Laboratory (shown in Fig. 1). A portion of the proton beam extracted from the accelerator interacted in the Meson Center (MC) target which was used by two other beam lines. About half the beam to the Meson Laboratory was transmitted through the MC target and down the *M*2 beam line to the dump target. The *M*2 beam was focused to ~4 mm on the face of the dump target.

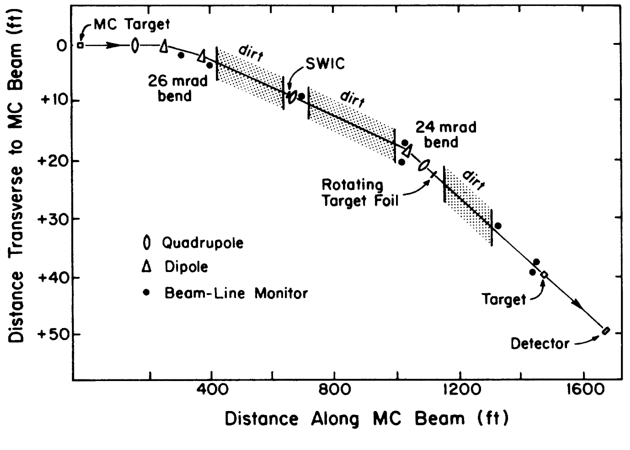

FIG. 1. Plan view of the *M*2 beam line upstream of the experiment showing the MC target, the two bends leading to the dump target, and the positions of the beam-line monitors, of the SWIC, and of the rotating foil used to measure the halo background.

In order to minimize backgrounds from the beam and the MC target, the *M*2 beam was designed with two bends of ~25 mrad each. A series of three collimators located at the first bend point served to redefine the 400-GeV proton beam and to remove halo particles. Thus, the neutrinos produced in the upstream sections would be directed well away from the detector. No discernible flux was seen in the detector because (i) less than $\frac{1}{2}\%$ of the nonprompt ν flux is produced at angles exceeding 25 mrad and (ii) the solid angle subtended by the detector from the last bend point is $\lesssim 0.1$ that by the dump target. A gross test of the halo measurements and background estimation was performed by operating both with and without the MC target and noting that the observed flux was unchanged, although the statistical error in this measurement precluded a definitive test. Similarly, the beam was operated at low intensity ($\sim 1\%$ high intensity) but detuned so that the measured halo flux was comparable to that in the high-intensity beam. No events were observed whereas 22 would have been expected if all the ν_μ events observed in normal running conditions were due to upstream sources.

In addition to the reduction of background by design, beam conditions were continuously monitored and abnormal beam spills were rejected. Twenty-six monitors (typically, a coincidence of two photomultipliers each coupled to a quartz Cherenkov radiator) were positioned along the beam line to measure the beam losses and halo interactions. These monitors were calibrated by inserting foils of known thickness into the beam at several points and recording the loss of beam and halo that ensued (details in Sec. III A) (Ref. 12).

The beam flux in each pulse was measured using a secondary-emission monitor (SEM) located just upstream of the target. Also installed in the beam was a segmented-wire ionization counter (SWIC) used to monitor the position and shape of the beam. The uncertainty of the SEM calibration was determined to be ±3% by inserting a number of copper foils in the beam and measuring the ^{24}Na activation. A typical beam pulse delivered 3×10^{12} protons to the dump target with occasional pulses of 5×10^{12} protons.

B. Dump targets

It is advantageous to use as dense a target as possible, since the greater the density, the shorter the effective decay length and, thus, the greater the suppression of nonprompt background. We chose to construct a target using a tungsten alloy ($A = 178$, density $= 19.2$), despite the disadvantage of low heat conductivity, which limited the proton flux on the target to $\sim 6\times10^{12}$ protons per spill. Practically, however, the primary limitation of the proton-beam intensity was imposed by radiation safety considerations and not by the tungsten target.

The technique of eliminating nonprompt background by extrapolation to zero absorption length requires targets of varying density made of the same material. A partial-density tungsten target was constructed of tungsten discs with spacing approximately twice the disc thickness (12.5 mm), resulting in a density about one-third the nominal density. The segmentation is small compared to the absorption length in solid tungsten (~ 100 mm), so that the target should appear homogeneous.

In addition to the two tungsten targets the target assembly incorporated a beryllium target, a copper target, and two partial-density copper targets, which were used to measure the dependence of charm production on atomic weight. The dimensions of the target hall precluded the use of a partial-density beryllium target greater than 2.5 absorption lengths. The effort required to obtain data with the partial-density Be target could not be justified given the limited beam time and systematic uncertainties in using a target of this length. Instead two partial-density copper targets were constructed in order to measure the consequences of finite target length.

A schematic view of the target-assembly area is shown in Fig. 2. The various targets were embedded in a water-cooled copper block, which could be manipulated by remote controls to insert a specific target into the beam. The characteristics of the several targets are listed in Table I.

Because of the finite length of the targets, the hadronic showers produced by the proton interactions are not always completely contained within the targets. This spillover of the shower into the iron or copper which backed up each target caused an increase (or decrease) in the nonprompt background depending on the target density. We have parametrized this effect by calculating an effective density (i.e., the density of an infinite-length target which produced the same nonprompt neutrino rate). For example, behind the full-density tungsten target were 3.9 absorption lengths of copper, which is less dense than tungsten, so the effective density is reduced relative to a long W target whereas the partial-density tungsten target was backed by the solid iron magnet so the effective density was larger than the nominal value (Fig. 2).

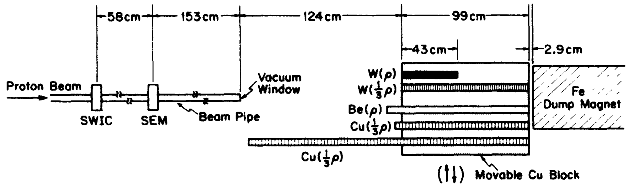

FIG. 2. A schematic view of the target block assembly showing the upstream SEM and SWIC, the relative lengths of the various targets, and the iron magnet downstream. The target block can be remotely moved to center each target on the beam.

A calculation of the ν flux from nonprompt sources was used not only to obtain the effective densities, but also to analyze the ν_e events as described below. The calculation was made using two independent techniques, direct integration and Monte Carlo methods, and the results were in good agreement. Measurements of the meson production cross sections for thick targets made of different materials are sparse. Data obtained with thin targets must be corrected to include multiple interactions (cascading), which have a greater effect on the π- and K-meson production than on charm production because the latter has a stronger energy dependence. Moreover, measurements of the dependence of meson production on the atomic weight A have not been made at our beam energy of 400 GeV.

The spectra of meson production by 400-GeV protons have been measured by Atherton *et al.*[13] using a $\sim 1\lambda_{\text{int}}$ beryllium target and can be cast in analytic form using a simple parametrization. It is apparent in Fig. 3 that the data for $\pi^{\pm}$ and $K^{\pm}$ are well described by the parametrization. The ratios of π to K production for 400-GeV protons on BeO targets have also been reported by Blain *et al.*[14] and their data are shown together with those of Atherton *et al.* and the parametrization in Fig. 4.

The major uncertainties in the calculation of the background flux are the correction for thick target effects, i.e., cascading, required for all targets and the effect of the A dependence of the production cross sections on data using the heavy targets. The data of Barton *et al.*[15] are the highest-energy results available on the A dependence of meson production. This dependence is conventionally written as $\sigma \propto A^{\alpha}$. These data, together with the data on the A dependence of K^0 ($\bar{K}^0$) production by 400-GeV protons,[16] and the results of two-parameter fits are shown in Fig. 5. The resultant systematic error of the calculation affects the overall normalization of the background for heavy targets and was estimated to be ~25%. The relative errors in the other fluxes (ν_μ:$\bar{\nu}_\mu$:ν_e:$\bar{\nu}_e$) were smaller, ~10%. The effective densities which result from

TABLE I. Target characteristics (absorption lengths λ_{abs} are for protons).

Target material	Relative density	Effective density	Length (mm)	λ_{abs}	Diameter (mm)
W	1.00	0.93	432	4.43	25
W/3	0.33	0.38	330	3.39	25
Cu	1.00	1.00	950	6.09	41
$\text{Cu}/2.4\vert_{\text{long}}$	0.42	0.42	895	5.74	41
$\text{Cu}/2.4\vert_{\text{short}}$	0.42	0.50	436	2.79	41
Be	1.00	1.00	1118	2.56	67[a]

[a] The cross section of the Be target was square rather than circular.

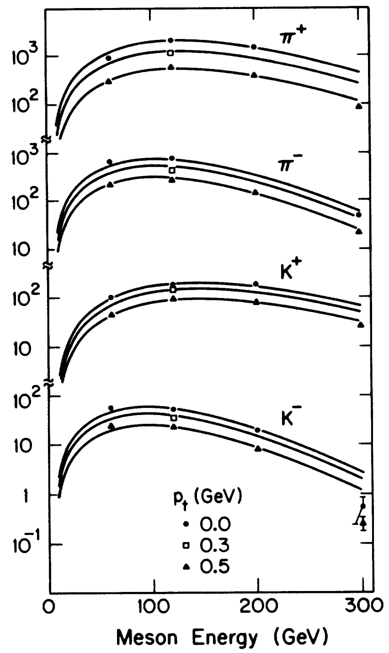

FIG. 3. The particle fluxes [particles/sr $(\delta p/p)$ proton] as measured by Atherton *et al.* (Ref. 13) for a thick (500-mm) Be target. The lines are the calculation of the fluxes determined in a fit to thin-target measurements and extrapolated to the thick-target yields.

this calculation are listed in Table I.

The correction for the effects of finite target length was experimentally checked by measuring the prompt muon rate using the two different length copper targets (details are given in the Appendix). The agreement of the measurements and the calculation of the effective density provides assurance that the correction for finite target length is well understood.

The tungsten target as noted was 25 mm in diameter, a compromise between the desire to facilitate the transfer of heat into the copper block and the need to ensure that the prompt neutrinos are produced within the tungsten. A calculation indicated that no significant ν flux ($E_\nu \geq 20$ GeV) was produced outside the tungsten target. To check this calculation the target block was moved relative to the beam and the particle flux, consisting mostly of muons which pass through the shield, was measured on beam center line. As shown in Fig. 6, the muon flux from the full-density tungsten target is reduced compared to its value in the copper block, whereas it is enhanced in the partial-density tungsten target. The transition occurs at the edge of the target and the slope is consistent with the beam width as measured in the SWIC. We conclude that our measurement is insensitive to interactions occurring outside the target. The beryllium and copper targets also need no correction. This muon flux exiting the shield was monitored continuously throughout the experiment to ensure proper targeting conditions.

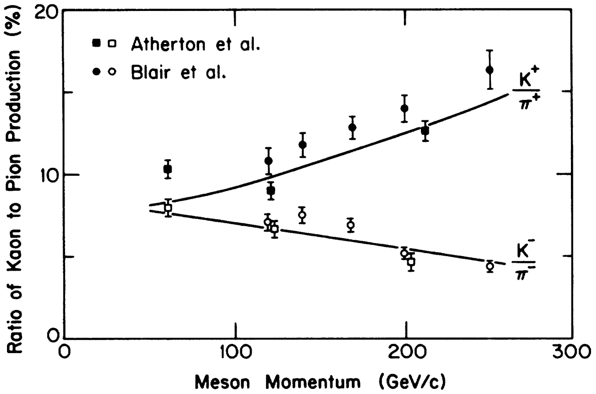

FIG. 4. The ratio of the production of K mesons to that of π mesons as measured by Atherton *et al.* (Ref. 13) and the CCFRR group (Ref. 14), and the parametrization (solid line) used in the calculation of the hadronic cascade.

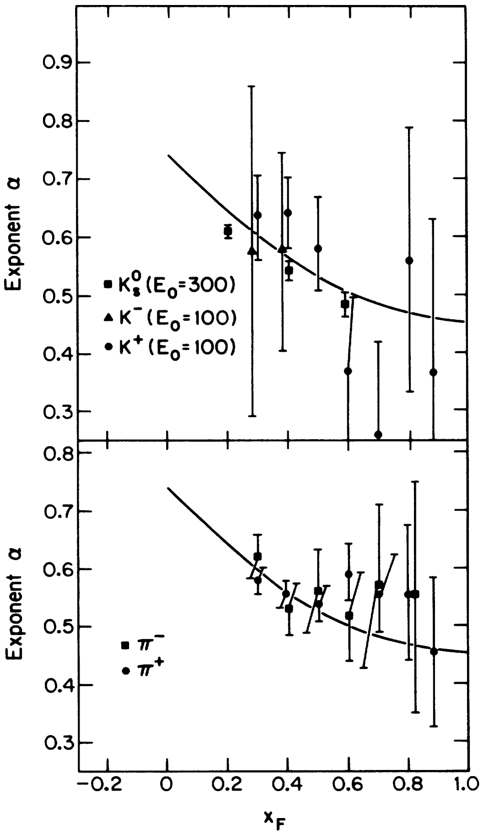

FIG. 5. The data of Barton *et al.* (Ref. 15) for π's and Skubic *et al.* (Ref. 16) for K's showing parametrizations (solid lines) of the dependence of the particle production cross sections on the atomic weight, $\sigma \propto A^\alpha$, where $\alpha = a + bx_F + cp_t^2 + dx_F^2$.

C. Muon shielding

In order to locate the detector near the target, it must be shielded from the large flux of muons ($\sim 10^9$ muons per spill). The conventional solution to this problem is to provide passive material sufficient to exceed the range of the highest-energy muons. The novel solution adopted

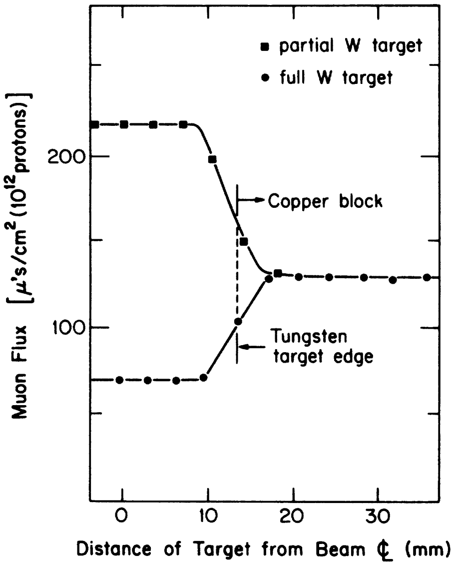

FIG. 6. The muon flux emerging from the active shield near beam center line as a function of the position of the proton beam on the tungsten targets. This flux measurement was used to ensure proper targeting throughout the experiment. The change in μ flux near the edge of the target is consistent with the 4-mm beam-spot size.

for this experiment was to provide an active shield which magnetically deflected the muons away from the detector. This active shield is shown in Fig. 7 and consisted of five solid iron magnets located downstream of the dump target. The magnets are sized such that μ's deflected toward the detector in the return yokes of the first two magnets are deflected away by the central region of the third magnet. Its return yoke in turn is shadowed by two magnets ("spoiler magnets") installed above and below the beam axis. The total bending power along the beam is 23.1 T m, which deflects muons with momentum <80 GeV/c away from the detector. The ionization energy loss in passing through this active shield is ~ 17 GeV. The computer-generator trajectories of four representative μ^- are shown in Fig. 7.

The flux of muons of momentum exceeding 80 GeV/c was negligibly small. However, multiple Coulomb scattering, trident production, and muons deflected toward the detector in the return legs of the magnets resulted in a substantial residual low-energy muon flux through the detector. This residual muon flux directed toward the detector was further attenuated by a passive shield of unmagnetized iron located between the active shield and the detector. Figure 8 shows the active and passive shield for data run 2. For the data run 1 iron blocks, shown as dotted lines, were used instead of shields 2 and 3, so the muon shielding, particularly in the forward direction, was less effective. The AVIS magnet was in place for all data runs but was not magnetized.

The flux rate (largely due to residual muons) in the three planes of scintillation counters located directly in front of the calorimeter (Fig. 9) was measured to be 3.4×10^4 (1.2×10^5) muons per spill for run 2 (1). The variation of this residual flux in the bending direction is shown in Fig. 10 where the muon flux density [μ/cm^2/(10^{12} protons)] was measured at the horizontal beam position as a function of the height above the floor. The results for both shields are shown together with the fluxes calculated by Monte Carlo techniques.[17] The agreement is qualitatively satisfactory, but the quantitative description of the residual flux is exceedingly difficult. When the muon flux is reduced by 4–5 orders of magnitude, as in our shield, rare processes become important, e.g., large-angle Coulomb scattering, trident production, variation of magnetic fields, cracks in the shield, etc.

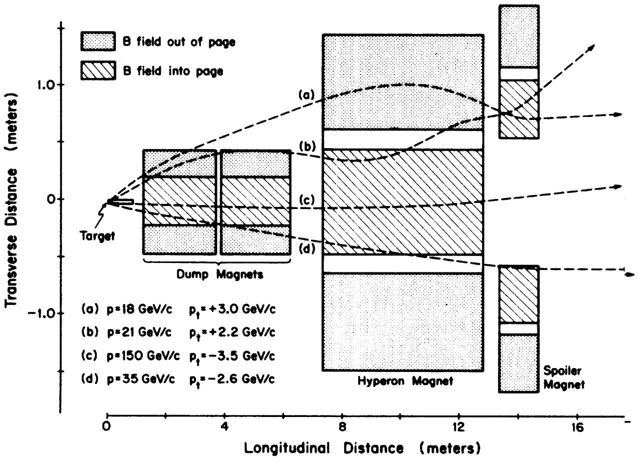

FIG. 7. A vertical section through the active muon shield showing the target-block assembly, the iron-core dump magnets, the hyperon magnet, and the spoiler magnets. Four μ^- trajectories (a)–(d) are shown which illustrate the complications resulting from the return-flux deflection. Only muon (d) intersects the detector.

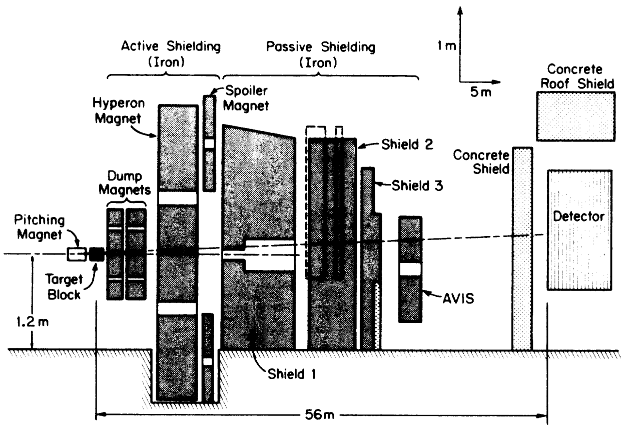

FIG. 8. A vertical section through the experiment showing the muon shielding, both active and passive, for run 2. For run 1, iron blocks, shown by the dotted lines, were used in place of shields 2 and 3. The gap in shield 1 was a 400-mm-diameter beam-pipe setup for a previous experiment.

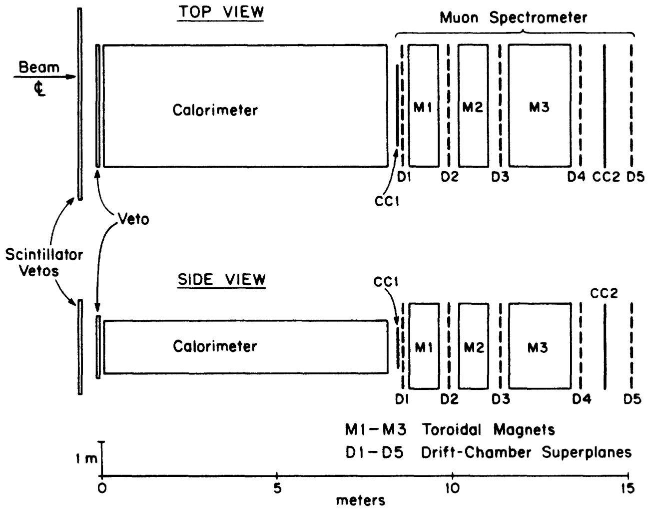

FIG. 9. A top view and a side view of the detector showing the front vetoes, the CC trigger counters (CC1 and CC2), the solid iron toroidal magnets ($M1$–$M3$), and the five superplanes of drift chambers ($D1$)–($D5$). Each superplane is composed of five individual drift-chamber planes (x,x',y,y',u).

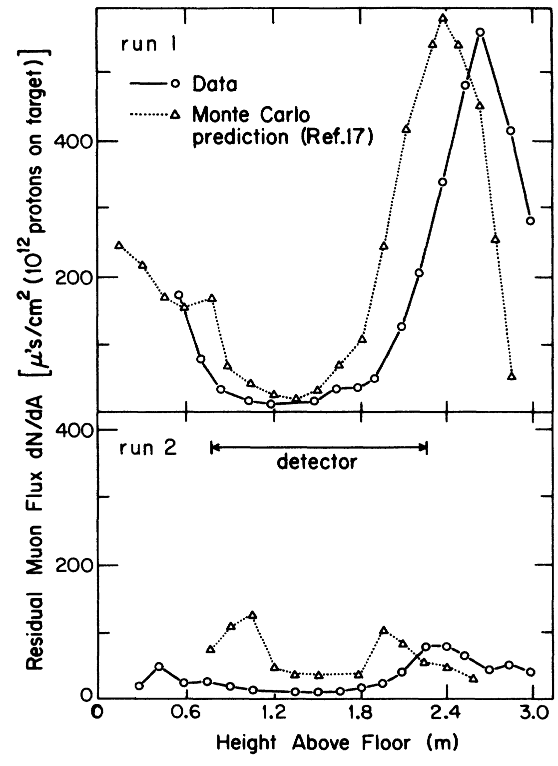

FIG. 10. The residual muon flux for the full-density tungsten target at the front face of the detector is shown at beam center line as a function of height above the floor for both the run-1 and -2 shields. The results of a Monte Carlo calculation by Oh (Ref. 17) are superimposed showing general agreement.

D. Detector

The neutrinos were detected by their characteristic interactions within the detector. Among the quantities which must be well measured are the energy and the position of the neutrino event. It is also necessary to reject background events and to identify ν_μ CC events, ν_e CC events, and neutral-current (NC) events. Obviously, the greater the detector mass, the larger the number of detected neutrino events. A schematic diagram of the detector is shown in Fig. 11.

The front face of the detector was located 56 m from the target face. The center line of the detector was offset 0.76 m horizontally from the beam axis as shown in Fig. 11, which resulted in a maximum angular acceptance of 37 mrad. This is in contrast with the arrangement in the CERN experiments for which no neutrinos were detected beyond 2 mrad. Details concerning the definition and calculation of the acceptance are discussed in Sec. IV C below.

In front of the calorimeter modules are two planes of scintillation counters and a plane of liquid-scintillator counters which are operated in a veto mode to prevent the initiation of data recording by muons passing through the detector. The calorimeter was constructed of lead plates in liquid scintillator tanks and its total mass was about 155 metric tons. An advantage of the use of lead, apart from its density, was the substantial difference between the radiation length (5.6 mm) and the absorption length (183 mm). This difference resulted in electron showers which were shorter and more concentrated than hadron showers. We exploited this variation in response in order to distinguish ν_e CC events (Sec. IV F).

The calorimeter[18] was composed of 30 modules, each of which contained 12 lead plates ($305\times151\times0.64$ cm^3)

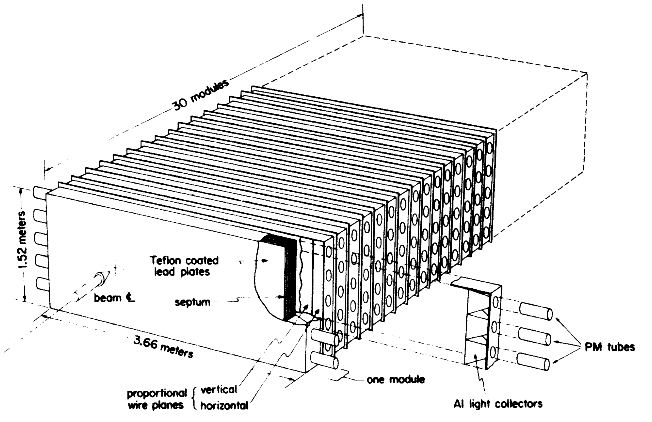

FIG. 11. An isometric view of the 30 Pb-liquid calorimeter modules which comprise the neutrino detector. Each module consisted of 12 Teflon-coated Pb plates ($305\times151\times0.64$ cm^3) in a tank of liquid scintillator. The tank was segmented vertically into five independent cells by septa, and each cell was viewed on either end by a Amperex 2202B photomultiplier tube. Between each module were crossed planes of proportional wire chambers.

spaced 6 mm apart (Fig. 11). The lead plates were covered with Teflon sheets which have a smaller index of refraction than the liquid scintillator. Thus the collected scintillation light was enhanced by total internal reflection. A module was divided into five cells by horizontal spacers. Each cell was viewed by an Amperex 2202B photomultiplier tube at each end. Behind each module two planes of proportional wire chambers[19] (PWC) were installed to measure the position and the spatial extent of the shower. The two planes had wires oriented orthogonally and spaced at 25-mm intervals. The thickness of each module and its two wire planes was 105.6 g/cm^2, mostly of lead. The energy resolution of the calorimeter was measured to be $\sigma(\text{hadrons}) \simeq 0.53\sqrt{E}$ (GeV) and $\sigma(\text{electrons}) \simeq 0.27\sqrt{E}$ (GeV) (Ref. 18).

Downstream of the calorimeter was a muon spectrometer (Fig. 9) composed of five drift-chamber superplanes and three toroidal magnets.[20] Each superplane contained two planes of vertical wires offset by half the wire spacing (100 mm) to resolve the left-right ambiguity, two planes of horizontal wires similarly offset, and one plane with wires rotated 30° with respect to the vertical.

The intrinsic resolution of the drift chambers was measured to be 0.25 mm. The magnets were constructed in the shape of a rectangular torus of dimension 3.7×2.4 m^2; the field strength was typically ~ 2 T and the total $\int B\,dl \sim 7$ T m.

Immediately after the calorimeter were two planes of scintillation counters (CC1). Another scintillator plane (CC2) was installed behind the muon spectrometer magnets. These planes were used in run 2 to trigger the apparatus on muons from ν_μ CC events.

E. Trigger

During run 1 the data acquisition was triggered solely on the basis of energy deposition in the calorimeter. The output signals from the photomultiplier tubes on each side of the detector were collected into 24 "segment" signals each consisting of the linear sum of 16 adjacent tubes. The segments were overlapping in order to ensure that no event was lost by the division of its energy across segment boundaries. The segment signal was then discriminated at both a high and a low level. The response (i.e., collected light) varied exponentially with distance from the phototube.[18] A trigger was generated if the calorimeter had a segment with a high level on one side and either a high or low on the other side. This definition produced an energy threshold for data recording which varied transversely across the calorimeter, from ~ 3.5 to ~ 7 GeV. For energy depositions ≥ 10 GeV the trigger efficiency was 95%.

It can be inferred from the exponential variation of the response across the cell that the product of the photomultiplier tube signals from opposite ends of a cell is independent of position. This allowed us to construct a trigger with an energy threshold independent of transverse position. For run 2 analog multipliers were developed[21] which computed the product of segment signals from opposite sides and discriminated the result. This trigger was independent of position and 95% efficient for energy depositions greater than 12 GeV.

During run 2 the data acquisition was also initiated by the outgoing muon from a ν_μ CC interaction in addition to the energy deposition trigger. This CC trigger was generated by the coincidence of the scintillator planes CC1 and CC2 with both sides of the calorimeter (Fig. 9). Its measured efficiency was 96% and it recorded those CC events which deposited small amounts of hadronic energy in the calorimeter, and hence failed to trigger on energy. This feature is particularly important for $\bar{\nu}_\mu$ interactions which deposit relatively less hadronic energy because of the $(1-y)^2$ dependence of the cross section.

Trigger rates, of course, depended strongly on beam intensity and target material. During run 2 the typical beam intensity was 3×10^{12} protons per 1-sec spill, which produced an average trigger rate of 32 Hz (24 from the energy trigger, 8 from the CC trigger). For this beam intensity and using the full-density tungsten target, the live time due to the scintillation veto counters was $\sim 89\%$ and the total live time, which includes the computer readout time, was $\sim 74\%$.

The trigger rate measured when the beam was off was ~ 7 Hz, attributable to cosmic rays. In order to measure the effect of this background a 1-sec gate was generated between beam spills to accept cosmic-ray data. Data analysis procedures for beam-on and beam-off gates were identical, so that events which occurred while the beam was off and which survived in the analysis represented the cosmic-ray background in the beam-on data. As will become apparent (Sec. IV F), cosmic-ray events were the source of almost no background to the ν_μ CC measurement and of very small background to the ν_e events.

III. UPSTREAM BACKGROUND

Despite the care taken in the design and tuning of the beam, there still remained a small background due to upstream sources. The causes of this background can be naturally separated into (i) beam halo produced by scraping or beam-gas interactions well upstream of the target; and (ii) interactions of the beam with material near the target (e.g., SWIC, SEM, air gap, vacuum window). With the monitors installed along the $M2$ beam we measured the beam halo and estimated the background due to (i). The background due to (ii) can be reliably calculated.

A. Beam halo

The beam halo was measured by inserting aluminum foils of known thickness into the beam just downstream of the final bend (Fig. 1). The counting rate with a foil of λ interaction lengths is $N(\lambda) = \alpha(\lambda + \lambda_0)$ where α is a constant and $\alpha\lambda_0$ is the rate due to beam-halo interactions. The ratio of counting rates with a foil inserted to that without a foil is independent of α:

$$R = \frac{N(\lambda)}{N(0)} = \frac{\alpha(\lambda + \lambda_0)}{\alpha\lambda_0} = 1 + \frac{\lambda}{\lambda_0} . \tag{3.1}$$

This is a straight line on a log-log plot: $\log_{10}\lambda = \log_{10}(R-1) + \log_{10}\lambda_0$. In Fig. 12 we plot the

TABLE II. Upstream beam-line material. The entries for p and L are typical values, which vary slightly from target to target. The correct values of their product are given for each target in the appropriate column.

Object	Interaction probability p	Decay length L (cm)	pL (relative ν rate) W	W/3	Cu	Cu/2.4$\vert_{\text{short}}$	Cu/2.4$\vert_{\text{long}}$	Be
SWIC	1.1×10^{-3}	348	0.390	0.420	0.400	0.424	0.300	0.440
SEM	0.9×10^{-3}	290	0.250	0.280	0.260	0.280	0.185	0.294
Vac window	0.1×10^{-3}	139	0.013	0.016	0.014	0.016	0.006	0.018
Air gap	1.7×10^{-3}	139	0.226	0.269	0.239	0.268	0.005	0.275

typical counting rates for several monitors. At $R=2$, λ_0 can be directly read off for each monitor; e.g., for monitor HM1301E at 1-μm beam-line pressure λ_0 is $\sim0.7\times10^{-5}$ absorption lengths.

The residual gas in the beam line was an important component of the upstream material which caused background. In Fig. 12 the counting rates in the monitors are plotted for a pressure in the beam line of 1 and 50 μm. The counting rates at 50 μm were roughly 7 times those at 1 μm. From measurements at other pressures, we determined that at 1 μm the beam-gas interaction was negligible. All beryllium data, most copper data, and more than half the tungsten data were taken with 1-μm pressure; the remainder with 10 μm ($\lambda_0\sim2.0\times10^{-5}$) λ_{abs}).

Similar studies of the background due to halo interactions occurring upstream of the final bend indicated a negligible contribution to the prompt rates in the detector. The measured rates in the halo monitors were comparable, but the bend in the beam line and the smaller solid angle subtended by the detector substantially decreased the effect. This upstream background can be compared to the nonprompt neutrinos produced by hadron decay within the target (the pion absorption length in tungsten is 124 mm). If we assume all the halo background arises at the last bend point, the decay path length is 113 m and the relative solid angle is $\sim\frac{1}{4}$. Hence, the halo background can be bounded:

$$\frac{\text{halo background}}{\text{nonprompt }\nu}\le(\tfrac{1}{4})(1\times10^{-5})\left[\frac{11\,300}{12.4}\right]$$

$$\le0.002\ . \qquad (3.2)$$

(In Table VI the nonprompt rate for the full-density tungsten target is 34.0 per 10^{16} protons, so the halo background was ≤0.07 events per 10^{16} protons.)

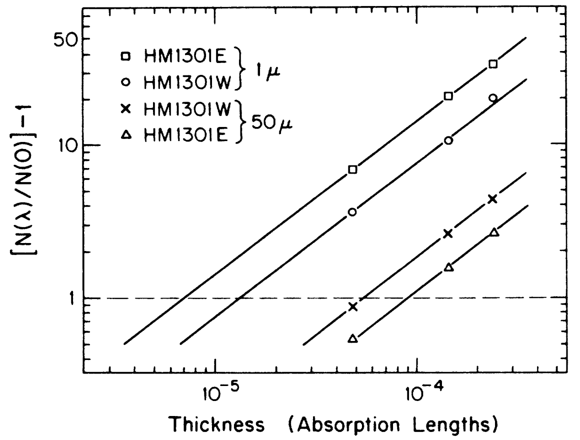

FIG. 12. The ratio of counting rates $[N(\lambda)/N(0)-1]$ as a function of absorber thickness λ for two of the halo monitors, each with beam-pipe pressures of 1μ and 50μ. The lower rate for 1μ pressure is clear. At $N(\lambda)/N(0)=2.0$ (horizontal dotted line), the effective interaction length λ_0 can be read directly on the x axis.

B. Beam-line material

Any material inserted into the beam upstream of the target will cause proton interactions and subsequent decays into neutrinos. The resulting flux will be independent of the target density and, thus, cannot be measured by extrapolation to zero-absorption length of the dump target. As shown in Fig. 2, a SWIC and a SEM were inserted just upstream of the target to measure the beam flux and monitor the focus. In addition, an air gap of ~120 cm existed between the vacuum window and the target. The upstream background is determined by the interaction probability and the subsequent decay probability (for π and K). It is, of course, different for ν_μ and $\bar{\nu}_\mu$ because of different production rates for $\pi^{\pm}$ and $K^{\pm}$.

The material in the beam line for run 2 is listed in Table II together with typical values of the interaction probability, decay length, and the relative background neutrino flux for each combination of source and target. The decay length is the sum of the true geometric length and the decay distance within a target ($\sim\lambda_{\text{abs}}$). Although the air gap has the largest interaction probability, a significant part of the neutrino production comes from the SWIC and SEM which are further upstream. The upstream background varies slightly from target to target (Table II).

In Table III the calculated number of neutrino events (flux$\times\sigma_\nu$) per 10^{16} protons due to this material is

TABLE III. Calculated number of events per 10^{16} protons due to upstream background in run 2 (3).

Target	ν_μ	$\bar{\nu}_\mu$
W	2.27 (3.34)	0.42 (0.62)
W/3	2.52 (3.70)	0.47 (0.69)
Be	2.73	0.51
Cu	2.35 (3.46)	0.44 (0.64)
Cu/2.4$\vert_{\text{long}}$	1.33	0.25

presented for the various targets. The run 1 rates (in parentheses) reflect a thicker vacuum window and a larger air gap. The number of prompt ν_μ ($\bar{\nu}_\mu$) events in tungsten for the large fiducial volume are 44±6 (21±3) events per 10^{16} protons on target (Sec. IV E). Hence, the flux due to upstream sources is $\sim 7\%$ ($\sim 3\%$) of the prompt ν_μ ($\bar{\nu}_\mu$) rate, which is less than the statistical error of the prompt rate.

IV. DATA ANALYSIS

A. Data selection

The trigger rate was typically 20–30 events per 1-sec spill, of which $\sim\frac{1}{3}$ were due to cosmic-ray interactions. Most of the remainder were due to interactions caused by the large flux of particles directed above and below the detector by the active magnetic shield. Only $\sim 0.3\%$ of the triggers are truly from ν interactions. The data selection must identify these ν-induced events with good efficiency.

The most important characteristic of neutrino events is that they are contained within the calorimeter, except for possible leakage out the back. Thus, a buffer zone was defined around the front and sides of the calorimeter in which no energy deposition was allowed. The front veto counters ensure, with better than 98% efficiency, that incoming charged particles cannot trigger the apparatus. High-energy neutrons were absorbed in the passive iron shield upstream of the detector. Since each module is approximately $\frac{1}{2}$ absorption length, energetic incident neutrons would interact preferentially at the front of the calorimeter, but no such variation was found.

One expects to identify with good efficiency the ν_μ CC events which have an easily recognizable μ passing through the spectrometer. However ν_e CC events have only a splash of energy in the calorimeter and are topologically indistinct from NC events as well as from some cosmic-ray interactions. Hence, we divide the data into two categories: 1μ events (those with a μ passing through at least three planes of the spectrometer) and 0μ (ν events without such a μ). Since we do not distinguish the beam-on and the beam-off data in the selection process, the cosmic-ray-induced background was found from the number of beam-off 0μ events which were selected.

In the first step of the selection process a few data runs were discarded which had anomalies in the beam-line monitors, target position, detector performance, etc. For the remaining runs, individual spills for which the monitors indicated abnormal beam-line conditions were rejected.

Next, several independent software programs were used to cull the raw triggers and to select events which had the topological features characteristic of neutrino interactions. In this first level the data sample was reduced by a factor of 16 by requiring that the energy trigger be reconstructed from the individual photomultiplier pulse heights, the energy deposition in both the calorimeter and PWC's be localized, the candidates not be cosmic rays (that is, the energy flow must be aligned along beam direction), the candidates not be showers originating from interactions in the floor or roof, and the candidates not be incoming muons.

The second level featured more restrictive criteria by incorporating information from the PWC's, whose 25-mm grid and two-dimensional readout provide better resolution than the liquid-scintillator modules. In this level the sample size was reduced by a factor of 3 by the requirements that the energy deposition span at least two adjacent calorimeter modules, the maximum energy deposition occur within 4 modules of shower origin, and a consistent vertex be present in both PWC dimensions.

These criteria were successful in identifying with good efficiency a 0μ event sample, but have some biases against 1μ events; for example, a μ with a downstream electromagnetic shower could have a disjoint energy deposition and, thus, be rejected. However, the CC trigger installed for run 2 required very little energy deposition in the calorimeter and the resultant 1μ events were not identified with these programs. Consequently, a third-level program was developed which used only the PWC information to reconstruct the μ tracks originating in the calorimeter.

Once the candidates had been selected by the programs, they were displayed graphically and independently examined by two physicists. Events selected were classified as either 1μ or 0μ and a correct vertex was assigned. In Fig. 13 the information available and the format for typical 1μ and 0μ events are shown. Events designated as quasielastic [Eq. (5.15)] were removed and analyzed separately (Sec. V F).

The 1μ visual scan efficiency was measured by double scanning a large fraction of the W data. The total number of 1μ events found in the selected sample was 635; each scan found 634 so the efficiency was $\sim 100\%$ (most of the W data was scanned twice).

The efficiency of the 1μ selection program was estimated by comparing the results of program selection with those selected in a visual scan of events tagged by the CC trigger. In a subset of the Be data, 671 1μ events were found visually and the program found 98% of these.

To determine the efficiency of finding 0μ events in the analysis, the μ track was artificially removed from a 1μ event (by removing the PWC and calorimeter hits from the data record) and the remaining data record was denoted a "pseudo 0μ" event. These "pseudo 0μ" events were inserted randomly at the appropriate statistical level into data runs, which were then passed through the standard selection process. The 0μ selection programs found (89±1)% of these incognito "pseudo 0μ" events. The subsequent double visual scan found (95±1)% of the events selected by the programs. There was no evidence of bias in energy. The overall 0μ efficiency for the run 1 analysis was 0.77 and for run 2 was 0.88.

Two different fiducial volumes were designated because of the different topologies of 1μ and 0μ events (see Table IV). The "large" fiducial volume, used primarily for 1μ events, required the vertex to be no closer than 20 cm to the calorimeter edges (frontal area 264×111 cm^2) and to be within modules 3–26. The resultant fiducial mass is 75 tons.

In order to remove the contamination of the 0μ sample caused by the leakage into the sides of the calorimeter, a

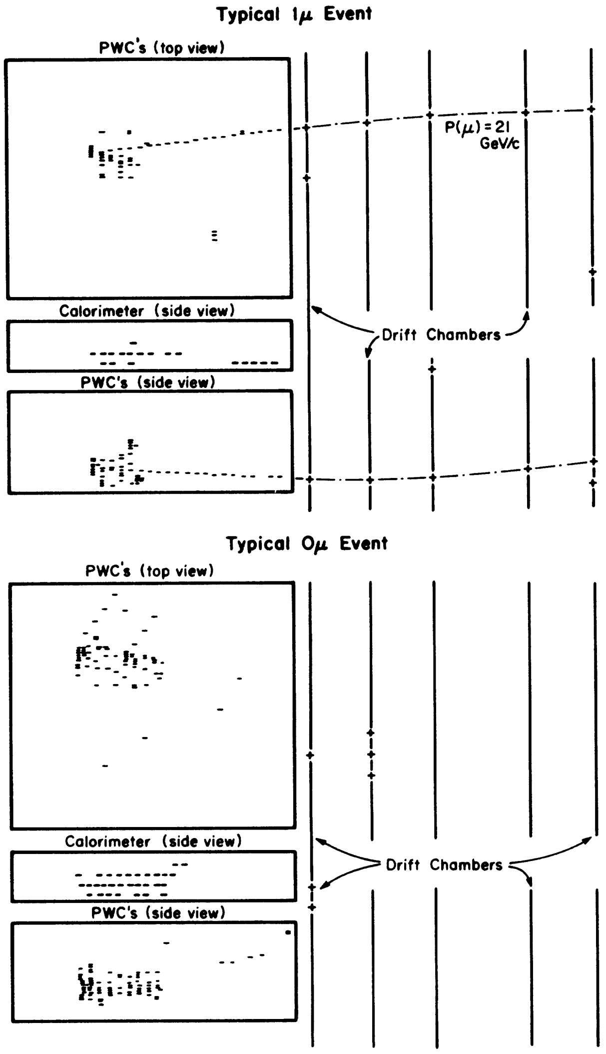

FIG. 13. Pictorial view of typical 1μ and 0μ events showing the calorimeter energy deposition the PWC hits in both top and side views, and the drift-chamber hits. The 1μ event also shows a fitted μ track.

slightly greater restriction on the transverse location of candidate vertices was imposed by a "small" fiducial volume. It was defined in part by a conical projection from the target position to an area (244×111 cm^2) at the rear of module 26 (Ref. 22). Furthermore, the construction of the calorimeter modules incorporated four Al spacer bars to separate the horizontal cells (Fig. 11). Within the 25-mm region occupied by these spacer bars the calorimeter was insensitive. While this had little effect on hadron showers, which were widely dispersed, it seriously biased the measurement of energy for ν_e events with a vertex inside the spacers. It is estimated that $\sim$30% of ν_e events occurring in the spacers would incorrectly fail to pass the energy threshold criterion $E_\nu \geq 20$ GeV (Ref. 23). Hence, 0μ events were excluded if the vertex lay within the spacers. These two constraints defined the "small" fiducial volume of mass 63 tons.

B. Measurement of muon momentum

The μ momentum was reconstructed from the drift-chamber hits using an algorithm[22] that incorporated the energy loss in the toroidal iron magnets. This procedure determined the momentum of the muon as it left the calorimeter. Fitting losses due to the fringe B field near the toroid holes were 1% and were corrected. The most probable fitting residual was 0.65 mm; virtually all residuals were less than 2 mm. Typical muon momentum errors were $\delta p/p=0.12$ for low-energy ($p_\mu \sim 5$ GeV) and 0.22 for high-energy ($p_\mu \sim 100$ GeV) muons. The low-energy momentum error is dominated by multiple scattering in the iron toroids, whereas the high-energy error comes from the bending power of the B field.

The muon, of course, loses energy by ionization in traveling from the vertex to the point at which it exits the calorimeter. In addition, because of the short radiation length of the lead calorimeter, significant energy can be deposited along the trajectory of high-energy muons due to radiative processes. Such energy deposited in the calorimeter which could be associated with the muon was removed from the evaluation of the hadron energy and

TABLE IV. (a) Summary of 1μ data obtained using the large fiducial volume (rates per 10^{16} protons on target corrected for detector acceptance). (b) Summary of 1μ and 0μ data obtained using the small fiducial volume (rates/10^{16} protons on target corrected for detector acceptance and efficiency).

Target	W	W/3	Cu	Cu/2.4$\vert_{\text{long}}$	Be
			(a)		
Protons (10^{16})	13.7	3.9	2.7	0.8	7.7
ν_μ CC events	769	398	201	126	777
$\bar{\nu}_\mu$ CC events	277	130	65	29	191
ν_μ CC/10^{16}	90.6±3.3	162.5±7.7	122.3±8.7	226.8±19.1	229.5±10.0
$\bar{\nu}_\mu$ CC/10^{16}	30.8±1.9	47.9±4.0	32.1±4.1	47.0±8.4	63.4±5.5
			(b)		
ν_μ CC/10^{16}	71.0±2.9	128.4±6.8	93.8±7.0	164.5±15.9	
$\bar{\nu}_\mu$ CC/10^{16}	24.3±1.7	37.6±3.5	25.3±3.6	40.5±7.5	
0μ events	1026	366	193[a]	122	958
0μ/10^{16}	89.0±2.9	128.8±6.7	103.9±7.6	178.7±16.4	155.3±4.8

[a] The 0μ Cu events come from 2.1×10^{16} protons.

was added to the momentum of the muon as measured in the spectrometer.

C. Determination of ν energy

The hadronic and electromagnetic energy deposited in the calorimeter by the neutrino interaction was measured using the photomultiplier pulses. Because the scintillation light was exponentially attenuated in the direction transverse to the beam, the product of the pulse heights observed on opposite ends of a cell was independent of the position of the shower.[18] For most cells a comparison of the pulse area to that observed for the most probable energy loss for a muon was used to convert to the "number of equivalent particles" (NEP's). The calibration of the calorimeter in a hadron beam of known energy was then used to normalize the response in GeV.

Occasionally, the energy deposition in a cell would be so small or so large that one of the phototube signals would have a nonlinear response. When this occurred, the energy in the cell was calculated from the other phototube output using the attenuation length and the vertex as measured by the proportional wire chambers.

Since a hadronic shower produces $\sim 80\%$ as much light as an electromagnetic shower of the same energy, it is necessary to incorporate the composition of the shower in the estimation of its energy. Clearly, since one goal of this experiment is to distinguish ν_e CC events from NC events, the determination of shower composition can be of great utility. The use of lead in the calorimeter, which has a radiation length much shorter than the absorption length, facilitates this separation. Hence, electromagnetic showers are much shorter (~ 1 module) than hadronic showers (~ 6 modules). Interactions of hadrons in the calorimeter were observed to deposit on the average about half their energy in the first module. Details of the measurements and the analysis are given elsewhere.[18] The energy deposited in the first module of the shower is defined as E_{em}; the energy in the remaining modules is denoted E_2; and the total energy $E_{\mathrm{tot}}=E_{\mathrm{em}}+E_2$. From the profile of module energies we know that the hadronic energy E_{had} can be calculated from E_2: $E_{\mathrm{had}}=\zeta E_2$ where $\zeta \approx 2$. A variable y_s was defined: $y_s=E_{\mathrm{had}}/E_{\mathrm{tot}}$. For a pure electromagnetic shower $y_s \sim 0$, and $y_s \sim 1$ for a pure hadronic shower. For ν_e CC events y_s is an approximation to the scaling variable y.

In terms of this parameter the neutrino energy can be expressed as

$$E_\nu(y_s)=\frac{E_{\mathrm{tot}}(\mathrm{NEP})}{5.56(1.0-y_s)+4.40y_s}\ \mathrm{GeV}\ , \tag{4.1}$$

where 5.56 and 4.40 are calibration constants measured for electromagnetic and hadronic showers, respectively. We note that for lower-Z calorimeters used in other experiments this technique of distinguishing electromagnetic energy is less decisive because the characteristic lengths are more nearly equal.

The energy calibration of the calorimeter was periodically monitored during the experiment using the muon flux through the detector. (The distribution of channel calibration had a $\sigma \sim 5-7\,\%$). Of course, the data were analyzed using the most recent calibration.

D. Acceptance

We divide the acceptance correction into two parts. The first (detector acceptance) is the probability that a neutrino which interacts within the fiducial volume will be accepted by our analysis procedure. It contains the energy threshold effect of the trigger and the solid-angle acceptance of the muon spectrometer. The second (geometric acceptance) is the probability that a neutrino will interact within the fiducial volume of our detector.

The detector acceptance depends only on the neutrino energy E_ν and $\mathbf{r}$, the vertex position of the neutrino interaction. It can be expressed by the following integral over the range of hadronic energy E_h and the angle of the μ, $\xi=1-\cos\theta_\mu$:

$$A(E_\nu,\mathbf{r})=\int \frac{d^2\sigma}{dx\,dy}\frac{\partial(x,y)}{\partial(E_h,\xi)}T(E_h)A_\mu(E_h,\xi)d\xi\,dE_h\ . \tag{4.2}$$

As input we require (1) the neutrino cross section $d^2\sigma(x,y)/dx\,dy$ in terms of scaling x and y; (2) the Jacobian $\partial(x,y)/\partial(E_h,\xi)$ to convert from scaling x,y variables to variables that are directly measured by the detector, E_h and ξ; (3) the trigger efficiency $T(E_h)$ as a function of hadronic energy; and (4) the acceptance of the muon spectrometer $A_\mu(E_h,\xi)$ as a function of the muon energy $E_\mu=E_\nu-E_h$ and the angle ξ. The integration limits are determined by the kinematic boundaries of E_h and ξ. Details of the integration are presented in Ref. 22. The acceptance weight, $A^{-1}(E_h,\mathbf{r})$, for each observed event was summed to obtain the total corrected number of neutrino interactions.

The muon acceptance, $A_\mu(E_h,\xi)$ is the probability that a muon produced by a neutrino interaction at $\mathbf{r}$ intersected at least three superplanes of drift chambers. In practice, this was calculated by defining a fiducial box[22] at the end of the calorimeter, which depended not only on $\mathbf{r}$, but also on the muon momentum and the relative sign of the muon charge and the magnetic field. For those muons with sufficient energy to pass through the first two iron toroids the acceptance is simply the fraction of the cone (defined by the angle between μ and the detector center line) contained within this box.

In Fig. 14 the energy dependence of the muon acceptance for CC events is plotted for the two data runs; this shows the increase in acceptance (particularly for $\bar{\nu}_\mu$) resulting from the addition of the CC trigger for run 2. The muon acceptance for CC ν_μ ($\bar{\nu}_\mu$) interactions in the detector with $E_\nu \geq 20$ GeV was 0.63 (0.63) for run 1 and 0.78 (0.86) for run 2. The detector acceptor was also obtained using Monte Carlo techniques with results in agreement with those of the acceptance weighting method.

The geometric acceptance $G(\theta_\nu)$ depended only on the angle between the incident proton and the outgoing neutrino, θ_ν. As Fig. 15(a) shows, for $\theta_\nu \leq 10$ mrad the geometric acceptance is 1. However, for θ_ν between 10

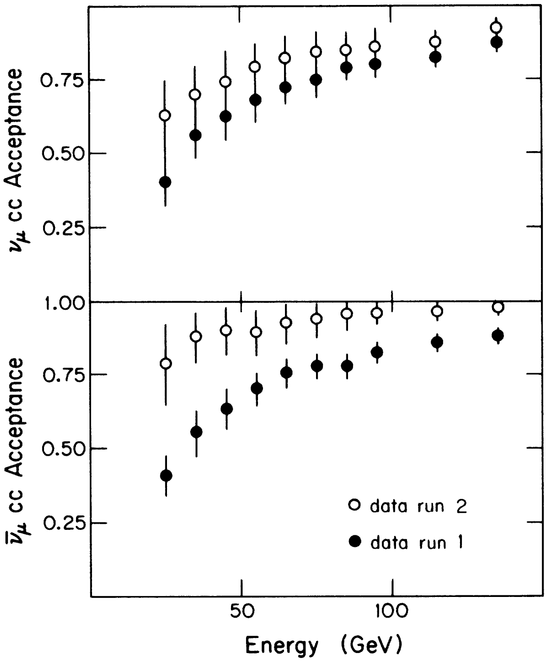

FIG. 14. Energy dependence of the ν_μ and $\bar{\nu}_\mu$ acceptance for run-1 and -2 data samples. The improvement in run 2 was due to the installation of the CC trigger.

and 30 mrad only $\sim 20\%$ of the neutrino events are detected, due simply to the partial azimuthal coverage. In Fig. 15(c) the dotted lines show the effect of detector constraints ($E_\nu \geq 20$ GeV, $\theta_\nu \leq 30$ mrad) on the neutrino $p_\perp$. It is clear that neutrino events with high $p_\perp$ are not rejected by the energy threshold limit of 20 GeV.

Since $\theta_\nu \leq 10$ mrad for much of the neutrino flux [Fig. 15(b)], the geometric acceptance has relatively little effect on the total number. However, it does depend on the neutrino production process and so the correction must be evaluated in terms of a specific model of charm production. For the model described below (see Sec. V E)

$$E_D \frac{d^3\sigma}{dp_D^3} \propto (1-x_F)^{3.2} e^{-1.5 p_\perp} , \tag{4.3}$$

the acceptance for $E_\nu \geq 20$ GeV as a function of $p_\perp$ is nearly constant ($\sim 12\%$ as shown in Fig. 16). For Feynman $x_F \geq 0.4$ more than 80% of the charm-decay neutrinos enter the calorimeter as shown in Fig. 16. This is in contrast to the CERN beam-dump neutrino experiments for which $\sim 2\%$ of these neutrinos entered the detector.

E. Calculation of prompt $\nu_\mu + \bar{\nu}_\mu$ CC event rates

The prompt (P_i) and nonprompt (N_i) neutrino rates for tungsten are calculated from the measured full- (F_i) and partial- (T_i) density CC rates as follows:

$$\begin{aligned} F_i^- &= P_i^- + N_i^- , \quad T_i^- = P_i^- + \rho_i^- N_i^- , \\ F_i^+ &= P_i^+ + N_i^+ , \quad T_i^+ = P_i^+ + \rho_i^+ N_i^+ , \end{aligned} \tag{4.4}$$

where i denotes seven energy (or $p_\perp$) bins into which the data were divided and the superscript specifies the charge of the muon (ν_μ or $\bar{\nu}_\mu$ events). The ρ_i parameter is the ratio of effective densities for the full- and partial-density targets, as determined in the hadronic-shower calculations (Sec. II). The energy dependence of the ρ_i parameters is small ($\sim 3.5\%$). This set of 28 equations with 28 unknowns is an unconstrained system. The least-squares solution is equivalent to an independent extrapolation in density for each energy bin and is given in Table V.

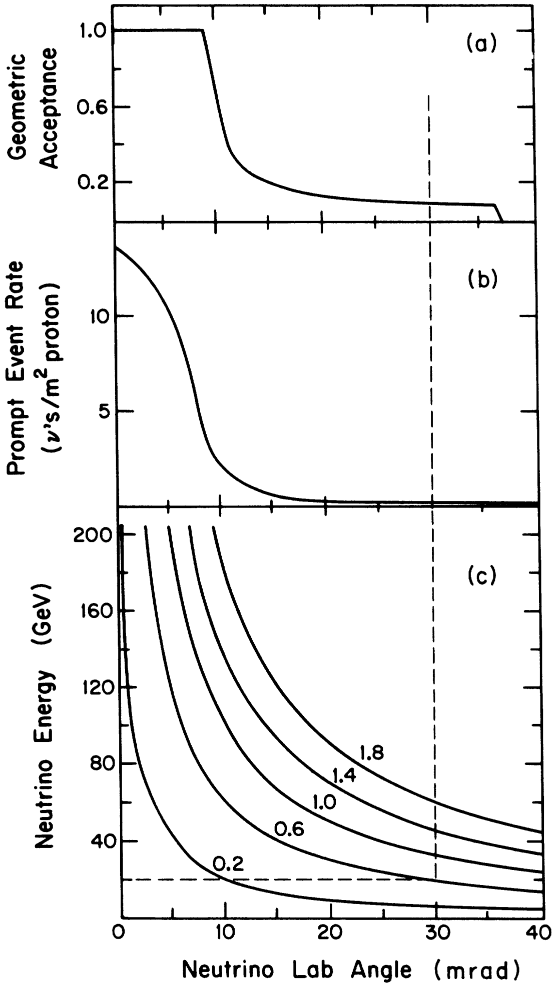

FIG. 15. (a) The geometric acceptance of the detector as a function of the angle between the incident proton and the outgoing neutrino; (b) the angular distribution of neutrinos expected from charm production $E_D d^3\sigma/dp_D^3 \propto (1-x_F)^{3.2} e^{-1.5 p_\perp}$ measured by this experiment; (c) curves of constant $p_\perp$ as a function of energy and angle. The dotted lines show the experimental limits of the detector.

The background values determined in this independent extrapolation show large statistical fluctuations (Fig. 17). A smoother energy variation results by incorporating in the analysis information obtained from the hadronic shower calculation concerning the energy spectrum of the nonprompt ν spectra and the ratio of nonprompt $\nu_\mu/\bar{\nu}_\mu$. In this modified procedure the total background rate is still determined by extrapolation. The shape of the energy spectrum is imposed by the relations

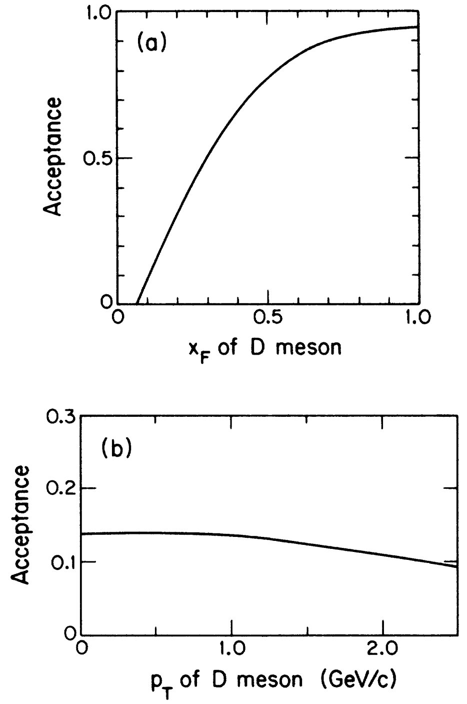

FIG. 16. The acceptance for charm neutrinos with $\theta_\nu \leq 30$ mrad and $E_\nu \geq 20$ GeV as a function of (a) x_F (Feynman x) of the D meson and (b) $p_\perp$ of the D meson.

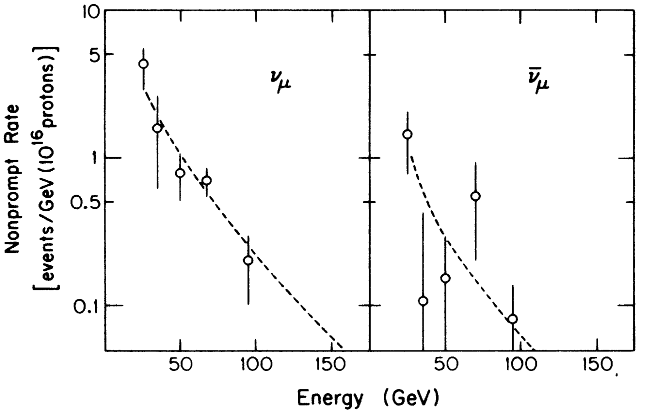

FIG. 17. Nonprompt ν_μ and $\bar{\nu}_\mu$ rates as a function of energy as determined in the solution of Eq. (4.4). The dashed line represents the calculated rates normalized to the total number of ν_μ events as measured in the overall extrapolation (e.g., Fig. 18). The $\bar{\nu}_\mu$ rate is then determined using the calculated ratio.

$$N_i^{\pm} - f_i^{\pm} \sum N_j^{\pm} = 0 \; , \tag{4.5}$$

where $\sum N_j$ is the total number of nonprompt ν events and the f_i are the fraction of events in each energy bin as determined in the hadronic shower calculations. Similarly, the ratio of nonprompt $\bar{\nu}_\mu/\nu_\mu$ calculated using the measurements of the π^-/π^+ and K^-/K^+ ratios in 400-GeV proton interactions is imposed as

$$N_i^+ - rN_i^- = 0 \; , \tag{4.6}$$

where $r = 0.19 \pm 0.04$. In Fig. 17 the values of the nonprompt rates determined in the unconstrained extrapolation [the solution of Eq. (4.4)] are shown together with the values determined in the modified analysis. The ν_μ flux is determined from the data, and the $\bar{\nu}_\mu$ flux is constrained by the calculated ratio. The agreement between the unconstrained values of the background flux and those determined using the calculated shapes is good.

The inclusion of these additional equations increases their number to 49 with the same number of unknowns. As noted this procedure has the effect of smoothing statistical fluctuations in the energy distributions, particularly for $\bar{\nu}_\mu$ data, albeit with the introduction of systematic error. The errors obtained in the analysis incorporated the uncertainties in the parameters f_i and r by weighting each constraint equation with the inverse of its estimated error.

The prompt neutrino rates measured in both the small and large fiducial volumes are presented in Table V for a variety of extrapolation procedures and the values are seen to be quite stable, independent of the choice of analysis.

In Fig. 18 the measured and extrapolated ν_μ and $\bar{\nu}_\mu$ rates are shown for the full- and partial-density tungsten and copper targets. By use of the extrapolation procedure, as noted above, not only the prompt rates but also the nonprompt rates are determined. The nonprompt rates were also calculated using the hadronic cascade in the target, a calculation identical to that used in the estimation of the effective density (Sec. II B). Us-

TABLE V. Prompt ν_μ and $\bar{\nu}_\mu$ rates per 10^{16} protons for several extrapolation procedures.

		Small fid. vol.		Large fid. vol.	
Constraint	Target	ν_μ	$\bar{\nu}_\mu$	ν_μ	$\bar{\nu}_\mu$
Unconstrained	Tungsten	33.4±6.6	15.7±3.7	43.6±7.4	19.7±4.1
Shape	Tungsten	35.5±3.8	17.4±2.1	44.5±4.3	21.3±2.4
Nonprompt ratio	Tungsten	33.0±6.4	16.5±2.9	42.9±7.2	20.9±3.2
Ratio and shape	Tungsten	34.4±5.3	17.1±2.6	43.7±6.0	21.4±2.9
Unconstrained	Copper	43.3±16.5	14.5±8.2	47.7±20.2	21.5±9.3
Shape	Copper	70.6±11.1	21.0±4.0	64.2±11.1	19.8±4.0
Nonprompt ratio	Copper	56.2±19.5	20.0±7.2	51.7±19.5	19.1±7.2
Ratio and shape	Copper	62.4±16.0	22.6±6.3	56.8±16.0	21.5±6.3

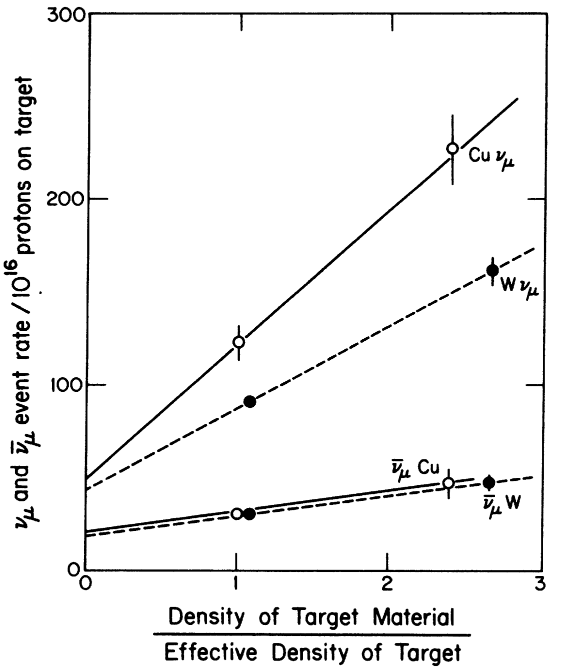

FIG. 18. The ν_μ and $\bar{\nu}_\mu$ CC rates for copper and tungsten targets showing the extrapolation to prompt rates. The larger nonprompt flux (steeper slope) observed in copper data due to the lower density is apparent, as is the smaller nonprompt flux in the $\bar{\nu}_\mu$ data (shallow slope).

ing the proton elasticity of 0.3 and computating to 5 generations, we calculated the neutron flux with $E_\nu \geq 20$ GeV from π and K decays which entered the calorimeter. The results of this calculation are compared with the values measured by extrapolation in Table VI. The calculated fluxes are somewhat larger ($\sim 30\%$). We attribute this difference to the difficulty of quantitatively modeling the A dependence of the meson fluxes and of extrapolating data taken with thin targets to thick targets. If the calculated fluxes are renormalized by the ratio of the measured ν_μ rate for the full-density W target to its calculated value ($R_{\text{norm}} = 0.704$), the remaining nonprompt rates are in excellent agreement with their measured values as shown in Table VI.

F. Calculation of prompt $\nu_e + \bar{\nu}_e$ CC event rates

The prompt $\nu_e + \bar{\nu}_e$ CC events constitute roughly half the sample of 0μ events and must be distinguished from a background of (1) cosmic-ray interactions; (2) ν_μ and $\bar{\nu}_\mu$ CC events with an unidentified μ; and (3) neutral-current (NC) events (either ν_e or ν_μ). Two independent methods were used to extract the $\nu_e + \bar{\nu}_e$ flux (1) the subtraction of known backgrounds from the 0μ data; and (2) the identification of the outgoing electron using the longitudinal shower profile of each event.

Selection based on the shape of the shower as observed both in the calorimeter and the PWC eliminates virtually all beam-off events (Sec. IV A). The beam-off gate monitors the number of cosmic-ray events that slip through the procedure. No muon events and only $\sim 2\%$ of the final 0μ data sample occurs within the beam-off gate; in the tungsten data there were 1026 0μ events in the ongate and 23 in the offgate.

In the subtraction method we estimate the rate of 0μ events per 10^{16} protons produced by each of the background processes for seven different energy bins and subtract it to arrive at the $\nu_e + \bar{\nu}_e$ CC rate. This is, of course, correct only on average, so it is not possible to identify specific background events.

By far, the largest background comes from ν_μ and $\bar{\nu}_\mu$ events (both CC and NC). We emphasize that, since the background does not depend on the source of the neutrinos, it is unnecessary to distinguish prompt and nonprompt neutrinos. Thus, all observed ν_μ events (not only the nonprompt) are used to normalize the calculated correction. Furthermore, since the nonprompt $\nu_e + \bar{\nu}_e$ are a small fraction of the prompt $\nu_e + \bar{\nu}_e$ (see Table VII), an extrapolation measurement similar to the ν_μ (Fig. 18) is unnecessary and the nonprompt $\nu_e + \bar{\nu}_e$ rates were calculated explicitly and subtracted. The corrected prompt rates for the full- and partial-density targets were compared to provide an independent check of the consistency of the subtraction procedure.

The largest component of the correction to the 0μ rates arises from the $\nu_\mu + \bar{\nu}_\mu$ events in which no μ is identified. The calculation of both $\nu_\mu + \bar{\nu}_\mu$ CC and NC background comes directly from knowing the detector acceptance $A(E_\nu, \mathbf{r})$ for each 1μ event. The ν_μ events not detected will remain in the 0μ data if $E_{\text{had}} \geq 20$ GeV. Once the weighting technique determines the true number of $\nu_\mu + \bar{\nu}_\mu$ events, the number of NC events is calculated from the NC/CC ratio ($R_{\text{NC/CC}} = 0.3$) and the energy threshold. Table VII shows the $\nu_\mu + \bar{\nu}_\mu$ subtractions for each of the targets.

In addition to the $\nu_\mu + \bar{\nu}_\mu$ NC events, the 0μ data contain $\nu_e + \bar{\nu}_e$ NC events. We assume that $R_{\text{NC/CC}}(\nu_e) = R_{\text{NC/CC}}(\nu_\mu) = 0.30$ and determine

TABLE VI. Comparison of the nonprompt shower calculation with measurements for ν_μ and $\bar{\nu}_\mu$ rates/10^{16} protons (large fiducial volume). For the nonprompt ν_μ in W the measured and normalized are required to be identical. The ratio 33.8/48.0 is then used to normalize the remaining data.

Target	Meas.	Nonprompt ν_μ Calc.	Norm.	Meas.	Nonprompt $\bar{\nu}_\mu$ Calc.	Norm.
W	33.8	48.0	33.8	6.0	11.5	8.1
W/3	85.0	119.9	84.4	15.2	28.6	20.1
Cu	55.5	74.0	52.1	9.7	10.3	7.3
Cu/2.4$\vert_{\text{long}}$	130.1	178.0	125.3	22.8	25.1	17.7

TABLE VII. 0μ subtraction rates per 10^{16} protons.

Target	W	Cu	Be
0μ event rate	89.0±2.9	103.9±7.6	155.3±4.8
$\nu_\mu+\bar{\nu}_\mu$ CC background rate	16.8±0.7	21.0±1.3	46.5±2.1
$\nu_\mu+\bar{\nu}_\mu$ NC background rate	14.6±0.2	18.4±0.5	41.4±0.7
$\nu_e+\bar{\nu}_e$ NC background rate	7.3±0.3	7.8±0.9	7.4±0.7
$\nu_e+\bar{\nu}_e$ nonprompt rate	3.9±0.3	6.6±0.9	18.1±1.3
$\nu_e+\bar{\nu}_e$ prompt rate	46.2±3.0	50.2±7.8	41.9±5.4

$dN/dE(\nu_e\ \text{CC})$ by solving the integral equation using the observed energy spectrum of the 0μ events remaining after the subtraction of ν_μ backgrounds:

$$\frac{dN}{dE}(\text{obs})=\frac{dN}{dE}(\nu_e\ \text{CC}) +R_{\text{NC/CC}}(\nu_e)\int_E^\infty \frac{dE'}{E'}\frac{d\sigma}{dy}\bigg|_{y=E/E'} \times\frac{dN}{dE'}(\nu_e\ \text{CC}) . \quad (4.7)$$

Because the observed energy for ν_e NC events is only E_{had}, the number of $\nu_e+\bar{\nu}_e$ NC events above our 20-GeV threshold is ~16% of the ν_e CC events.

The $\nu_e+\bar{\nu}_e$ CC so determined are both prompt and nonprompt. The nonprompt $\nu_e+\bar{\nu}_e$ events come from K (and μ) decays, but not from π decays, so the correction is much smaller than for $\nu_\mu+\bar{\nu}_\mu$. Using the shower calculation of nonprompt background described in Sec. IV D and normalizing the absolute flux by the constant found for ν_μ ($R_{\text{norm}}=0.704$), the nonprompt $\nu_e+\bar{\nu}_e$ rate per 10^{16} protons is determined for each target (Table VII).

As a check on the nonprompt calculation it is possible to estimate the nonprompt $\nu_e+\bar{\nu}_e$ rate by using the spectrum of ν_μ and $\bar{\nu}_\mu$ which come from $K_{\mu 2}$ decays. Since the daughter neutrino is massless, the angular distribution in the laboratory frame is independent of the decay mode so the neutrino acceptance of the detector for different decay modes is identical. By assuming that the production rate of K^0 equals that of K^+ and $\bar{K}^0$ equals that of K^-, we can directly calculate the nonprompt $\nu_e+\bar{\nu}_e$ rate using the parent-child relation:[24]

$$\frac{dn}{dE}(K\rightarrow\pi e\nu) =3\frac{B(K^+\rightarrow\pi e\nu)}{B(K^+\rightarrow\mu\nu)}\int_{E'}^\infty \frac{dE'}{E'}\frac{1}{d\Gamma}\frac{d\Gamma}{dx}\bigg|_{x=E/E'} \times\frac{dN}{dE'}(K^+\rightarrow\mu\nu) . \quad (4.8)$$

The partial rate for K^0 is twice that for K^+ decay due to the $\Delta I=\frac{1}{2}$ rule, and the combined rate is thus three times that for K^+. The calculation is described in detail in Ref. 23 with results in agreement with those derived from the shower calculation. Hyperon decay does not contribute at all to the ν_e background, and although included in the $\bar{\nu}_e$ flux calculation, it contributes $\lesssim 5\%$ to the combined nonprompt background. Results of a calculation of the specific contributions made by each channel have been presented by Wachsmuth.[25]

Details of the determination of $\nu_e+\bar{\nu}_e$ flux by analysis of the longitudinal distribution of event energy are presented in Refs. 26 and 18, and the results are in agreement with those obtained using the subtraction method. However, because of shower fluctuations and small statistics, this method is somewhat less precise than the subtraction method.

G. Systematic errors

The precision of the experimental conclusions is indicated by the magnitude of the systematic error. The systematic uncertainties are determined separately for ν_μ and ν_e because the quantities enter differently in the analyses, as shown in Table VIII, in which they are given as a fraction of the measured result. The error in corrections calculated from measured rates is included in the statistical error, e.g., ν_μ corrections to the 0μ rates are reflected in the ν_e prompt rate errors, as presented in Table VII.

Therefore, in the measurement of the ratio ν_e/ν_μ, the errors for both ν_e and ν_μ contribute; in that of the A dependence predominantly those for ν_e contribute; and for $\sigma_{D\bar{D}}$, which is determined roughly by the average of the ν_μ and ν_e values, about half the errors of each contribute.

As discussed Secs. II and III an important goal of the design of the experiment was to minimize the uncertainties caused by upstream halo, beam line material, and target size. That transverse target size was not a problem is illustrate by Fig. 6 and discussed in Sec. II B. The determination of the false prompt ν_μ flux due to upstream beam halo is described in Secs. III A and III B.

The error in the effective density was estimated by Monte Carlo calculation and corroborated by the experimental measurement as discussed in the Appendix. In these Monte Carlo studies the parametrization of the nonprompt neutrino production was modified, and the resulting neutrino spectrum was compared to that used in the main stream analysis. Each quantity was varied by $\sim 1\sigma$ in the calculation to determine its contribution to the result. In some cases reasonable changes in the parametrization were performed, e.g., for the A^α dependence of the π and K production $\alpha(x_F)$ was set to a constant and the results were then calculated. In Sec. IV A we discussed the evaluation of the finding efficiencies.

TABLE VIII. Systematic errors.

Quantity	$(\nu_e/\nu_\mu)_{\rm W}$ (%)	A^αdep (%)	$\sigma_{D\bar{D}}$ (%)
Measurements			
Upstream background	1	0.1	0.5
SEM proton count		3	3
Effective target density	7		3.5
Nonprompt ν_e calculation	1	4	1
CC acceptance	5	2	3
Event-finding efficiency	5	5	3
E_ν determination	3	3	3
Energy dependence of $\sigma_{D\bar{D}}$			2
σ_ν on Pb			6
Branching ratio $D \to xe\nu$		0.1	10
Model dependence			
A^α: $\delta\alpha = 0.05$			26
$(1-x_F)^n$: $\delta n = 0.2$			6
$e^{-bp_\perp}$: $\delta b = 0.2$			0.9

V. RESULTS

A. $\bar{\nu}_\mu/\nu_\mu$ ratio

The flux ratio $\bar{\nu}_\mu/\nu_\mu$ for the tungsten target was calculated from the prompt event rates (P^+ for $\bar{\nu}_\mu$ and P^- for ν_μ) in the large volume. Since the neutrino detector is predominantly made of lead, for which the ratio of neutrons to protons (I) is 1.509, the observed flux ratio must be corrected:

$$\frac{\bar{\nu}_\mu}{\nu_\mu} = \left[\frac{P^+}{P^-}\right]\left[\frac{\sigma_{\nu p}}{\sigma_{\bar{\nu} p}}\right]\frac{1+RI}{1+\bar{R}I} , \tag{5.1}$$

where R ($\bar{R}$) is the ratio of the cross section[27-34] for ν_μ ($\bar{\nu}_\mu$) interactions on neutrons to that on protons, viz.,

$$R = \frac{\sigma_{\nu n}}{\sigma_{\nu p}} = 2.05 \pm 0.14, \quad \bar{R} = \frac{\sigma_{\bar{\nu} n}}{\sigma_{\bar{\nu} p}} = 0.52 \pm 0.03 . \tag{5.2}$$

Combining R and $\bar{R}$ with the isoscalar neutrino cross sections[35] we obtain $\sigma_{\bar{\nu} p}/E = 0.48 \pm 0.05 \times 10^{-38}$ cm^2 and $\sigma_{\bar{\nu} p}/E = 0.44 \pm 0.04 \times 10^{-38}$ cm^2. Thus the measured flux ratio becomes

$$\frac{\bar{\nu}_\mu}{\nu_\mu} = 2.3 \pm 0.2 \left[\frac{P^+}{P^-}\right] = 1.17 \pm 0.23 . \tag{5.3}$$

The prompt rates used in this evaluation were determined in a fit which used additional information concerning the shapes of the nonprompt ν_μ and $\bar{\nu}_\mu$ energy spectra and the relative number of $\bar{\nu}_\mu$ to ν_μ as described in Sec. IV F. If the prompt rates are determined by an unconstrained extrapolation, the result becomes ($\bar{\nu}_\mu/\nu_\mu = 1.08 \pm 0.29$). Alternatively, if the events are selected to be within the small fiducial volume, the ratio using the constrained fit becomes 1.20 ± 0.26; the unconstrained 1.13 ± 0.34.

Data taken with the copper target were also analyzed for the $\bar{\nu}_\mu/\nu_\mu$ flux ratio, although with reduced statistical significance. Since the detector (Pb calorimeter) is common to both the copper and tungsten measurements, we have only to insert the prompt rates for copper into Eq. (5.3). Incorporating the A dependence of meson production, we obtain the nonprompt ratio of $\bar{\nu}_\mu/\nu_\mu$ for copper, $r = 0.18$ which is reduced from the value $r = 0.19$ for tungsten (Sec. IV E). The result for copper data in the large fiducial volume is $\bar{\nu}_\mu/\nu_\mu = 0.91 \pm 0.37$ (1.08 ± 0.65) for the constrained (unconstrained) fit and in the small volume 0.87 ± 0.33 (0.80 ± 0.55) for the constrained (unconstrained) fit. A result based on analysis of the run 1 tungsten data has been previously reported.[36]

B. Equality of ν_e and ν_μ flux

From the hypothesis that the prompt neutrino flux is produced by the decay of charm particles, it follows that the flux of ν_e and ν_μ should be nearly equal apart from very small phase-space effects. As noted in the Introduction, previous experimental results from the CERN experiments had cast doubt on this equality, which led to speculations concerning alternative mechanisms for producing prompt neutrinos. In this experiment we find the prompt ν_e and ν_μ fluxes to be equal.[26]

Since ν_e and $\bar{\nu}_e$ cannot be distinguished in our data, it is impossible to compare the fluxes separately. However, because our measurement of $\bar{\nu}_\mu/\nu_\mu$, 1.17 ± 0.23, indicates an approximate equality between neutrinos and antineutrinos, we assume $\bar{\nu}_e/\nu_e \approx \bar{\nu}_\mu/\nu_\mu$ and compare event rates. For this comparison the tungsten data only were used, because they had the smallest background. All events, both ν_μ and ν_e, were required to occur in the small fiducial volume. The values of the prompt ν_μ and $\bar{\nu}_\mu$ rates were determined in the constrained fit as described in Sec. IV E, and the prompt $\nu_e + \bar{\nu}_e$ were determined using the subtraction method described in Sec. IV F. All events are corrected for detector acceptance and efficiency (Sec. IV D). No correction was needed for geometric efficiency, since the angular distributions of the prompt ν_e and ν_μ were observed to be essentially identical.

The weighted average of the prompt $\nu_e + \bar{\nu}_e$ event rate per 10^{16} protons for the full- and partial-density W targets is 50.3 ± 2.6 compared to the prompt $\nu_\mu+\bar{\nu}_\mu$ event rate of 51.5 ± 5.9, confirming the equality of ν_e and ν_μ fluxes. The ratio is $\nu_e/\nu_\mu = 0.95 \pm 0.12 \pm 0.18$. The rate asymmetry

$$A \equiv \frac{(\nu_e+\bar{\nu}_e)_{\rm CC}-(\nu_\mu+\bar{\nu}_\mu)_{\rm CC}}{(\nu_e+\bar{\nu}_e)_{\rm CC}+(\nu_\mu+\bar{\nu}_\mu)_{\rm CC}} = -0.027 \pm 0.064 \pm 0.04 \qquad (5.4)$$

provides a better mode of comparison than the ratio because the errors are Gaussian and symmetric. A slight improvement is obtained, if the neutral-current events are included in the rates. Let the subscript all signify the sum of neutral- and charged-current events, and the equality of the ratio of neutral to charged currents for ν_e and ν_μ is assumed. Then the asymmetry becomes

$$A \equiv \frac{(\nu_e+\bar{\nu}_e)_{\rm all}-(\nu_\mu+\bar{\nu}_\mu)_{\rm all}}{(\nu_e+\bar{\nu}_e)_{\rm all}+(\nu_\mu+\bar{\nu}_\mu)_{\rm all}} = -0.017 \pm 0.058 \pm 0.04 \ . \qquad (5.5)$$

As can be seen in Table IX the equality of ν_e and ν_μ is independent of neutrino energy. The errors obtained for the $\nu_\mu+\bar{\nu}_\mu$ event rates are consistently larger than those for the $\nu_e+\bar{\nu}_e$ event rates due to the loss of events whose muons miss the spectrometer and also to the systematic error in the correction of this loss.

C. Neutral-current-to-charged-current ratio for ν_e

From the analysis the ratio of neutral to charged currents for ν_e can also be determined. Let N_0 be the 0μ rate with the ν_μ events removed. Then N_0 is the sum of the ν_e charged and neutral events both prompt and nonprompt. It can be further written

$$N_0 = (1 + r_e \zeta)(\nu_e)_{\rm CC} \ ,$$

where r_e is the ratio of the neutral- to charged-current rates and ζ is the relative efficiency for detection of these rates due to the energy threshold. If we assume the ν_e and ν_μ fluxes are equal and account for the nonprompt ν_e rate, the result is $r_e\zeta = 0.107 \pm 0.12$. Finally, we can evaluate ζ using the $(\nu_\mu)_{\rm CC}$ and determine

$$r_e = 0.22^{+0.25}_{-0.22} \ .$$

Although poorly determined, this result is consistent with the value $r_\mu = 0.333$ obtained by weighting the values for ν_μ and $\bar{\nu}_\mu$.

D. A dependence of charm production

The dependence of charm production on atomic weight, $\sigma \propto A^\alpha$, can be investigated using targets of different materials. In general, nonperturbative models of heavy-quark production (e.g., diffraction) suggest an $A^{2/3}$ dependence, whereas perturbative QCD models require A^1. In practice, nuclear effects may alter this dependence as Halzen[37] has pointed out.

As previously discussed, the nonprompt $\nu_\mu+\bar{\nu}_\mu$ rates depend strongly on target density. Thus the prompt $\nu_\mu+\bar{\nu}_\mu$ rate in Be is a small fraction of the observed total rate. In this case the extrapolation technique would yield results of greatly reduced significance. Indeed it was for this reason that no partial-density beryllium target was installed.

We chose to compare the $\nu_e+\bar{\nu}_e$ prompt rate in the different targets since the nonprompt rate in the full-density Be target, although larger than that for tungsten, is still less than half the prompt rate (Table VII) and can be calculated and subtracted from the 0μ rates. In fact, the background calculations was most reliable for the Be target data, since the primary data on thick target meson production were taken using Be targets and no A-dependent extrapolation was necessary. The backgrounds were normalized to the observed distribution of ν_μ, both prompt and nonprompt. In Table VII the prompt $\nu_e+\bar{\nu}_e$ rates, uncorrected for geometric acceptance, can be seen to be approximately equal for Be, Cu, and W. This implies that the A dependence of charm production must be similar to that of the absorption cross section for protons on nuclei,[15] which varies as $A^{0.72}$.

Since the targets were restricted in size, some of the interactions, both primary and secondary, occurred beyond the boundaries of the target. For example, the Be target was $2.56\lambda_{\rm abs}$ in length (see Table I) so ~7.4% of the proton interactions occurred downstream in the iron magnet behind the target (Fig. 2). To the extent that charm production has a different A dependence than proton-nucleus absorption, this effect must be compensated. Table X shows the multiplicative correction necessary for each target assuming only the primary interaction produces charm. Clearly the corrections are negligible for $\alpha = 0.75$. For $\alpha = 1.0$ the Be rate is corrected by ~5%.

The index α which appears in the dependence of rate

TABLE IX. Comparison of prompt ν_e and ν_μ CC rates/10^{16} protons.

Energy (GeV)	ν_e CC prompt/GeV	ν_μ CC prompt/GeV	Asymmetry
20–30	1.06 ± 0.14	0.97 ± 0.37	0.04 ± 0.20
30–40	1.07 ± 0.12	0.91 ± 0.24	0.08 ± 0.14
40–60	0.53 ± 0.06	0.72 ± 0.14	-0.15 ± 0.12
60–80	0.35 ± 0.05	0.30 ± 0.10	0.07 ± 0.17
80–120	0.20 ± 0.02	0.25 ± 0.05	-0.14 ± 0.12
120–160	0.052 ± 0.013	0.065 ± 0.024	-0.11 ± 0.23
160–200	0.028 ± 0.01	0.030 ± 0.013	-0.03 ± 0.28

TABLE X. The effect on prompt rates of finite target length.

Target	Length (λ_{abs})	Correction for $\alpha=0.75$	Correction for $\alpha=1.0$
Be	2.56	1.004	1.047
Cu	6.09	1.000	1.000
W	4.43	0.9996	0.997

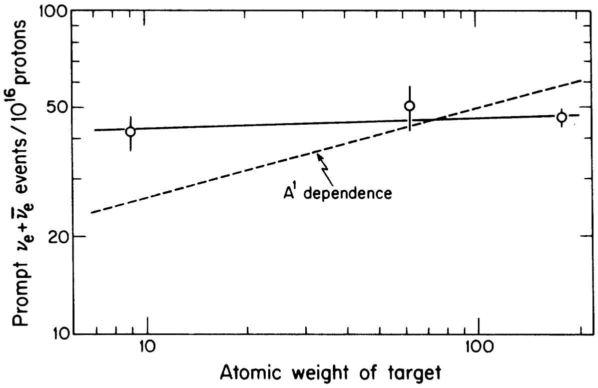

FIG. 19. The corrected $\nu_e+\bar{\nu}_e$ prompt CC event rate per 10^{16} protons as a function of the atomic weight of the targets: Be, Cu, and W. The solid line is a least-squares fit giving $\alpha=0.75\pm0.05$ with a $\chi^2=0.5$ for 2 DF. The dashed line is the best fit with the constraint $\alpha=1$ and has a $\chi^2=24.6$ for 1 DF. The $\alpha=1$ fit is corrected for finite target length.

on atomic weight $C \sim A^{\alpha-0.72}$ was determined in a least-square fit to the three data points ($\nu_e+\bar{\nu}_e$ prompt rates for Be, Cu, and W given in Table VII) with the result that

$$\alpha=0.75\pm0.05 \text{ with } \chi^2=0.5 \text{ for 1 DF} . \qquad (5.6)$$

In Fig. 19 the corrected prompt $\nu_e+\bar{\nu}_e$ CC rates and the result of this fit (solid line) are shown. The dashed line indicates the best fit to $\alpha=1$; $\chi^2=24.6$ for 2 DF. No significant energy variation of α was observed. We note that diffractive production occurs at large x_F and central production at small x_F; our acceptance is shown in Fig. 16.

Since our results were first published on A dependence[38] a similar result has been reported by the WA78 Collaboration[39] for charm production from incident pions by measuring the yield of single prompt μ: $\alpha(\mu^+)=0.76\pm0.08$ and $\alpha(\mu^-)=0.83\pm0.06$.

E. Charm-production cross sections

The cross sections for charm production were determined using the measured prompt ν event rates. The prompt $\nu_\mu+\bar{\nu}_\mu$ and $\nu_e+\bar{\nu}_e$ rates as a function of both energy and $p_\perp$ (Tables XI and XII) were summed. These data were corrected for geometric acceptance and corresponded to the measured neutrino event rates for $E_\nu \geq 20$ GeV and $\theta_\nu \leq 30$ mrad. The prompt $p_\perp$ spectrum comes from a 7-bin $p_\perp$ extrapolation fit analogous to the 7-bin energy extrapolation fit described in Sec. IV E. The resultant E_ν and $p_\perp$ distributions of prompt neutrinos are presented in Figs. 20 and 21.

The charm-production cross section is parametrized in terms of Feynman x and $p_\perp$ as

$$E_D \frac{d^3\sigma}{dp_D^3} \propto (1-x_F)^n e^{-bp_\perp} . \qquad (5.7)$$

Assuming that only $D\bar{D}$ pairs are produced, we compute the neutrino flux from the decay of the $D\bar{D}$ pairs, taking into account the detector acceptance ($E_\nu \geq 20$ GeV, $\theta_\nu \leq 30$ mrad) and the neutrino cross sections in Pb. We then fit the measured prompt neutrino rates as a function of energy and $p_\perp$ to Eq. (5.7). Although this experiment is sensitive only to neutrinos with $x_F \geq 0.2$ (Fig. 16), we assume symmetry about $x_F=0$ in the cross section.

In order to calculate the $D\bar{D}$ production from secondary interactions in the target it is necessary to make an assumption about the energy dependence. We assume an s^β dependence[40] with $\beta=1.3$. With this assumption our calculations indicate 6% of the charm production comes from lower-energy secondary particles in the hadronic cascade. Recent measurements at Fermilab[41] at 400 and 800 GeV indicate the energy dependence is $\beta=0.8^{+0.5}_{-0.4}$, a value consistent with our assumption but somewhat smaller. To the extent that β is smaller than 1.3, lower-energy protons are more effective at producing charm and the charm production by secondary pions may no longer be negligible. Using the pion parametrization previously described[13] our Monte Carlo calculations indicate the effect of secondary pions is still small. For $\beta=0.8$ charm production by secondaries becomes 7%; even for $\beta=0.3$ the secondary production is only 8%.

TABLE XI. Experimental dN/dE_ν spectra. Prompt CC neutrino rates per 10^{16} protons on tungsten (corrected for $\theta_\nu \leq 30$ mrad).

Energy (GeV)	$\nu_\mu+\bar{\nu}_\mu$ (events/GeV)	$\nu_e+\bar{\nu}_e$ (events/GeV)	$\nu_\mu+\bar{\nu}_\mu+\nu_e+\bar{\nu}_e$ (events/GeV)
20–30	2.45±0.97	4.64±0.6	7.09±1.17
30–40	2.81±0.61	3.16±0.51	5.97±0.84
40–60	1.75±0.29	1.53±0.23	3.28±0.37
60–80	0.57±0.15	0.79±0.15	1.36±0.21
80–120	0.36±0.07	0.34±0.06	0.70±0.09
120–160	0.105±0.030	0.068±0.019	0.173±0.035
160–200	0.019±0.008	0.014±0.004	0.033±0.009

TABLE XII. Experimental $dN/dp_\perp^2$ spectra for prompt CC neutrino rates per 10^{16} protons on tungsten (corrected for $\theta_\nu \le 30$ mrad).

$p_\perp$ (GeV/c)	$\nu_\mu+\bar{\nu}_\mu+\nu_e+\bar{\nu}_e$ [events/(GeV/c)^2]
0.0–0.2	257.2±39.5
0.2–0.4	174.7±19.6
0.4–0.6	113.9±14.8
0.6–0.8	53.2±8.3
0.8–1.0	36.2±5.9
1.0–1.4	9.0±1.8
1.4–2.4	2.2±5.4

Deducing a charm production cross section from a measurement of neutrino event rates requires knowledge of a chain of processes. The calculation of the neutrino flux can be understood in terms of a parent-child relation:[24]

$$2E_\upsilon \frac{d^3\sigma}{dp_\upsilon^3} = B_{D\to\nu} \int \frac{dx}{x} \left[\frac{1}{\Gamma_{D\to\nu}} \frac{d\Gamma_{D\to\upsilon}}{dx} \right] \times \int \frac{dE_D}{E_\upsilon} \left[2E_D \frac{d^3\sigma}{dp_D^3} \right] , \qquad (5.8)$$

where D refers to the charm particle; $\Gamma_{d\to\upsilon}$ is the decay rate into ν; $x=2E_\nu^*/M_D$; E_ν^* is the neutrino energy in the D rest frame; and $B_{D\to\upsilon}=0.101\pm0.010$ is the branching ratio[42] into neutrinos. The ν spectrum for semileptonic D decay has been measured in e^+e^- experiments[43] to be

$$\frac{1}{\Gamma(D\to\nu)} \frac{d\Gamma_{D\to\nu}}{dx} = 229.6x^{3.4}(1-0.943x)^{3.6} . \qquad (5.9)$$

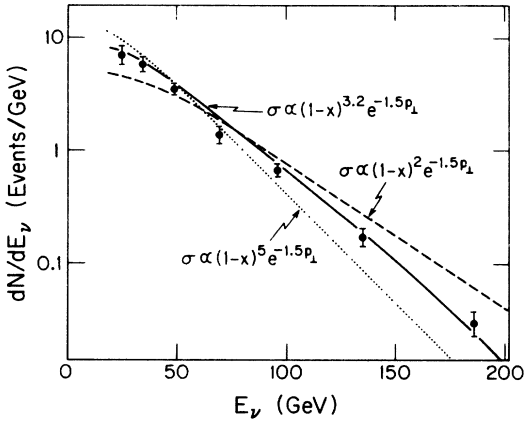

FIG. 20. Energy distribution dN/dE_ν of the measured prompt $\nu_\mu+\bar{\nu}_\mu+\nu_e+\bar{\nu}_e$ event rate per 10^{16} protons. The solid line represents the best fit to a $D\bar{D}$ production model (including detector acceptance) with $n=3.2$ and $b=1.5$. The dotted (dashed) line shows the spectra generated for $n=5$ ($n=2$).

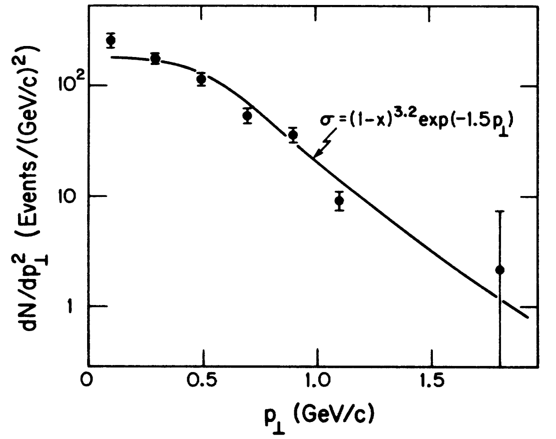

FIG. 21. Transverse-momentum distribution $dN/dp_\perp$ of the measured prompt $\nu_\mu+\bar{\nu}_\mu+\nu_e+\bar{\nu}_e$ event rate per 10^{16} protons. The solid line shows the best fit to a $D\bar{D}$ production model (including detector acceptance) with $n=3.2$ and $b=1.5$.

The observed differential neutrino spectra, dN/dE_ν and $dN/dp_\perp$, are calculated by the following integrals:

$$\frac{dN}{dE_\nu} = S \int_0^{30\ \mathrm{mrad}} 2\pi E_\nu \frac{d^3\sigma}{dp_\nu^3} \sin\theta_\nu d\theta_\nu , \qquad (5.10)$$

$$\frac{dN}{dp_\perp^2} = S \int_{20\ \mathrm{GeV}}^{\infty} E_\nu \frac{d^3\sigma}{dp_\nu^3} \frac{1}{E_\nu(E_\nu^2-p_\perp^2)^{1/2}} dE_\nu , \qquad (5.11)$$

where S is the effective neutrino cross section in Pb which takes into account both the different ν and $\bar{\nu}$ cross sections (assuming equal fluxes of ν and $\bar{\nu}$) and the nonisoscalar composition of Pb (see Sec. V A). The $D\bar{D}$ spectra are generated according to Eq. (5.7) for a specific value of n and b. As it turns out, the energy spectra (dN/dE_ν) are relatively independent of b, and $p_\perp$ spectra ($dN/dp_\perp$) are relatively independent of n. Hence the search for the correct n and b separates into two roughly independent procedures.

The detector acceptance is imposed on the calculated dN/dE_ν and $dN/dp_\perp^2$ and the resulting spectra are compared to the corresponding experimental spectra. We search for values of n and b which minimize the χ^2 of this comparison with the result

$$n=3.2,\quad b=1.5\pm0.2\ (\mathrm{GeV}/c)^{-1} , \qquad (5.12)$$

where $\chi^2=8.5$ for 12 degrees of freedom. The errors are determined at the 67% confidence level. In Fig. 20 the best fit spectra ($n=3.2$, $b=1.5$) are presented for both E_ν and $p_\perp$ as solid lines. To illustrate the sensitivity of these data to n we show, in addition, spectra for $n=5.0$ ($n=2.0$) by a dotted (dashed) line.

Incorporating the best fit spectrum for this parametrization with the observed A dependence (Sec. V C), we find the $D\bar{D}$ cross section

$$\sigma_{D\bar{D}} = 57.2\pm2.9\pm8.5\ \mu\mathrm{b/nucleon} , \qquad (5.13)$$

where the first error is predominantly statistical and the second is systematic, which is dominated by the uncertainty in the semileptonic branching ratio (see Table

VIII). This result agrees with other beam-dump experiments.[44] We emphasize that these results are derived predominantly from measurements of the ν_e rates and are relatively insensitive to details of the nonprompt ν_μ background.

Clearly, the assumption of only $D\bar{D}$ production cannot be completely correct, since many previous experiments have observed Λ_C production in hadron reactions.[45–50] To determine our sensitivity to $\Lambda_C\bar{D}$ production we choose a specific model in which the x_F distributions of the decay neutrinos are fixed to the values specified by quark counting rules[51] $\sigma_\nu(\Lambda_C\bar{D})\sim(1-x_F)^1$ and $\sigma_{\bar{\nu}}(\Lambda_C\bar{D})\sim(1-x_F)^3$. Repeating the previous analysis now assuming both $\Lambda_C\bar{D}$ and $D\bar{D}$ production with b fixed at 1.5 ± 0.2 $(\mathrm{GeV})^{-1}$ and the branching ratio[52] $B_{\Lambda\to\nu}=0.045\pm0.017$, we determine n for $D\bar{D}$ production and the cross-section ratio $\Lambda_C\bar{D}/D\bar{D}$ and find

$$\begin{aligned}&\sigma_{D\bar{D}}=63.7\pm10.0\pm9.0\ \mu\mathrm{b/nucleon}\ ,\\&\sigma_{\Lambda_c\bar{D}}=42.2\pm5.2\pm11.0\ \mu\mathrm{b/nucleon}\ ,\\&n_{D\bar{D}}=7.1\pm1.9\ ,\ \chi^2=6.5\ \text{for 18 DF}\ .\end{aligned}\tag{5.14}$$

This analysis is compared to the data in Fig. 22. We note that (i) $\Lambda_C\bar{D}$ production could be as much as 40% of the total charm production and remain consistent with our data; (ii) both models give about the same cross section for $D\bar{D}$ production. In general, however, production of F, Σ_C, etc., should be included but cannot be determined by the present data. Our inadequate knowledge of the branching ratios into neutrinos and spectra for charm particles other than D's ultimately limit the sensitivity of beam-dump experiments to a production mix of charmed particles. We conclude that the data provide a good measurement of $\sigma_{D\bar{D}}$ and are consistent with, but do not require substantial $\Lambda_C\bar{D}$ production.

F. Quasielastic neutrino rates

Events in which the neutrino scatters quasielastically ($\nu+N\to\mu^-+N'$) typically deposit small amounts of energy within the calorimeter and are characterized by small momentum transfer. Since the deep-inelastic structure functions are not appropriate for quasielastic events, such events must be identified and removed from the data sample of inelastic events. For data run 1 these quasielastic events were not accepted by the energy trigger. However, during data run 2 the CC trigger (Sec. II E) was efficient at detecting the muon from such events.

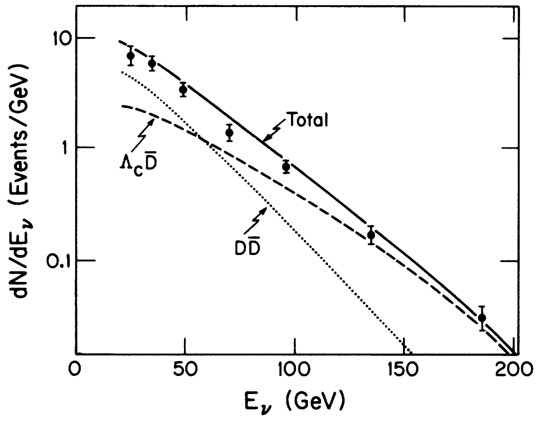

FIG. 22. Energy distribution of prompt $\nu_\mu+\bar{\nu}_\mu+\nu_e+\bar{\nu}_e$ events per 10^{16} protons. The solid line shows the best fit assuming both $D\bar{D}$ and $\Lambda_C\bar{D}$ production. The dashed (dotted) line shows the relative energy spectrum of the $\Lambda_C\bar{D}$ ($D\bar{D}$) events as determined by the best fit.

Thus, the quasielastic events must be removed from run 2. Furthermore, these events were used, in connection with previously measured quasielastic cross sections, to calculate the neutrino flux independently of energy. Since the inelastic cross section depends on energy, these two independent flux calculations provide corroboration of the energy calibration.

The data from the two runs on the tungsten targets were analyzed in an identical manner. The quasielastic events are separated from the inelastic events by restrictions on both Q^2 and W^2:

$$\begin{aligned}&Q^2=2Mx\nu<1.0\ \mathrm{GeV}\ ,\\&W^2=2M\nu+M^2-Q^2<3.5\ \mathrm{GeV}\ .\end{aligned}\tag{5.15}$$

A total of 57 (0) events were found in the run 2 (1) data sample for full- and partial-density tungsten targets as shown in Table XIII.

Since the calorimeter is not an isoscalar target (more neutrons than protons) an analysis similar to that of Sec. V A was used to account for the different cross section of neutrinos (and antineutrinos) on neutrons or protons. Using the nomenclature of Sec. V A the flux of neutrinos (f_{ν_μ}) is written

$$f_{\nu_\mu}=\frac{K_\nu(1+I)}{N\sigma_{\nu p}(1+RI)}\ ,\quad f_{\bar{\nu}_\mu}=\frac{K_{\bar{\nu}}(1+I)}{N\sigma_{\bar{\nu}p}(1+\bar{R}I)}\ ,\tag{5.16}$$

TABLE XIII. Comparison of neutrino flux measurements from quasielastic and inelastic interactions.

	Full density W		Partial density W	
	ν_μ	$\bar{\nu}_\mu$	ν_μ	$\bar{\nu}_\mu$
Number of quasielastic events	20	14	11	12
Number of corrected events	21.9	15.2	12.0	13.2
Flux/10^5 protons from quasielastics	3.7±1.2	4.1±1.9	6.8±3.6	26±13
Flux/10^5 protons from inelastic CC	4.5±0.5	3.6±0.5	8.3±1.1	5.2±1.1

where $N=1.45\times10^{27}$ nucleons/cm^2 in the fiducial volume and K_ν ($K_{\bar\nu}$) is the observed neutrino (antineutrino) charged-current rate per 10^{16} protons. Quasielastic cross sections have been reported by several bubble-chamber experiments[53–55] to be

$$\sigma_{\nu p}=0.7\pm0.1\times10^{-38}\ \text{cm}^2\ ,$$
$$\sigma_{\bar\nu p}=0.8\pm0.4\times10^{-38}\ \text{cm}^2\ . \tag{5.17}$$

Evaluation of Eq. (5.16) using these cross sections and the measured quasielastic rates results in the values of the neutrino (antineutrino) flux presented in Table XIII. The inelastic fluxes shown in Table XIII are derived by inserting the observed inelastic event rates and cross sections into Eq. (5.16) and integrating over energy >20 GeV. The values determined by the two calculations are consistent with a $\chi^2=4.5$ for 4 degrees of freedom.

G. Search for other sources

The characteristics of the prompt ν flux suggest that the production of charmed particles is their predominant source. Thus a search for other sources must contend with charm production as a background and, therefore, must be directed toward signals for which the charm contribution is small. Using the tungsten data we have made five measurements which could reveal the production of other heavy quarks, heavy leptons, supersymmetric particles or other new particles.

(i) The prompt flux ratio of ν_e to ν_μ is $0.95\pm0.12\pm0.08$ for events in the calorimeter with $E_\nu\geq20$ GeV/c (Sec. V B). Thus, the production of new particles resulting in either interactions or decays within the experimental volume which violate μ-e universality is limited. At 90% confidence level (C.L.) such a signal must be less than 0.21 of the prompt ν_μ CC events, i.e., less than 10 events per 10^{16} protons, or $\sigma\leq3.3$ μb/nucleon assuming $\sigma\sim A^{1.0}$.

(ii) The semileptonic decay of a particle more massive than charm would produce ν's at large transverse momentum. In the 0μ raw data sample we observe a total of 1.4 ± 1.0 events per 10^{16} protons with $p_\perp\geq1.5$ GeV/c. We expect that 3.6% of charm events (i.e., 1.8 events per 10^{16} protons) are produced in our detector with $p_\perp\geq1.5$ GeV/c. At 90% C.L., therefore, the upper limit for a signal is 1.3 events per 10^{16} protons.

(iii) A pure electromagnetic shower, i.e., a cascade with no hadrons, can be produced by the interaction or decay of new particles. Each of the calorimeter modules is 0.5 interaction lengths and 14 radiation lengths long, so that an electromagnetic shower is contained in ~2 or 3 modules. We examined the 0μ data sample for showers less than 4 modules in length and with no isolated tracks in the PWC and found 6.9 ± 1.2 events per 10^{16} protons. Of course, events of this type are to be expected from ν_e quasielastic scattering and from those deep-inelastic ν_e interactions which have a short shower length due to a fluctuation in hadronic content or cascade development. We estimated this expected contribution using the measured quasielastic ν_μ CC event rate.[53–55] The expected rate was determined to be 5.1 ± 0.8 events per 10^{16} protons. Thus the signal due to new particles is <3.5 events per 10^{16} protons at 90% C.L.

(iv) It is possible that particles which decay into electrons or muons might decay into a μ-e pair. By selecting those events with muons in which the shower was consistent with a pure electromagnetic shower, a rate of 1.5 ± 0.3 per 10^{16} protons was found (0.95 for ν and 0.59 $\bar\nu$). Although the background is difficult to estimate, this rate represents an upper limit to the signal for new particles.

(v) The data have been searched for interactions or decays in which only a pair of muons are produced with no accompanying cascade. No events were found. Several dimuons with hadronic energy were found, consistent with the number expected from decay of charm particles produced in ν interactions. The upper limit to the rate is 0.2 per 10^{16} protons at 90% confidence.

In summary, there is no evidence for the significant production of prompt ν's by other than charm particles at the levels indicated above. The significance of these limits can be discussed within the context of specific postulated particles. We have previously published details of a search for supersymmetric particles from this data.[56]

1. *B-meson production*

The B mesons (charge $\frac{1}{3}$ members of the third-generation doublet) decay semileptonically producing prompt ν's but with distributions dissimilar to those for charm. The distribution in $p_\perp$ for B mesons is considerably broader than for charm because of the greater Q value in the decay.

More quantitatively, for a charm production cross section of the form given in Eq. (5.7) then 3.6% of detected charm events occur with $p_{\nu\perp}\geq1.5$ GeV/c [$n=3.2$; $b=1.5$ (GeV/c)$^{-1}$]. Furthermore, if we assume the B-production cross section has the same form with $n=3.2$ (5.0), then 15.1% (11.7%) of B production would occur with $p_{\nu\perp}\geq1.5$ GeV/c [again $b=1.5$ (GeV/c)$^{-1}$]. Thus at the 90% confidence level the upper limit for the product of the B-production cross section and the ν branching ratio $\sigma_B B(B\to xl\nu)\leq1.3$ (1.6) μb/nucleon for an $A^{0.75}$ dependence of the cross section. For $\sigma\sim A^1$ the limit becomes $\sigma_B B\leq0.36$ (0.44) μb/nucleon. This limit does not test the theoretical expectation ~0.3 μb/nucleon ($0.005\sigma_{\text{charm}}$) because of the charm background, the statistical power of the experiment, and the uncertainties in the form of the cross section.

2. *Massive neutral lepton*

There is no *a priori* reason why neutrinos should be massless and a number of authors[57] have speculated on the existence of a massive neutral lepton L^0. We follow the analysis outlined by Gronau, Leung, and Rosner[58] in which massive neutrinos are assumed to mix with one flavor of light neutrino with left-handed ($V-A$) currents: namely, a heavy neutrino coupled to ν_μ or ν_e. We postulate that charm particles produced in the target decay into these heavy leptons: e.g., $D\to XeL^0$. The L^0 would then subsequently decay into leptons ($L^0\to l^+l^-\nu$) inside the fiducial volume of the detector. Hence limits on the production of the L^0 can be derived from the measurements (iii), (iv), and (v) above.

The expected number of L^0 decays per 10^{16} protons is given by

$$N_{L^0}=\frac{N_p B_{D\to XeL^0}(m_L^0,U^2)B_{L^0\to l^+l^-\nu}A(m_{L^0},E_{L^0},U^2)}{B_{D\to Xe\nu_e}A(\nu_e,E_\nu)}\,, \tag{5.18}$$

where $N_p=50.3\pm2.6$ is the prompt $\nu_e+\bar{\nu}_e$ event rate per 10^{16} protons; the B's are branching ratios; the A's are acceptances and U^2 is the mixing parameter. Since the acceptances for ν_e and L^0 enter as a ratio, the observed number of L^0 decays depends only weakly on the computational details. The semileptonic branching ratio is $B_{D\to Xe\nu_e}=0.101$ and the L^0 branching ratios ($B_{L^0\to e^+e^-\nu_e}=0.085$, and $B_{L^0\to\mu^+\mu^-\nu_\mu}=0.02$) are those predicted by the standard model.[58]

The acceptances were computed by Monte Carlo techniques assuming D production according to Eqs. (5.7) and (5.11). The decay probability of L^0 is calculable from the lifetime, which scales as $(m_\mu/m_{L^0})^5$:

$$\tau=4.15\times10^{-12}m_{L^0}^{-5.17}U^{-2}\ \text{for}\ \nu_e\ \text{coupling}\,, \tag{5.19}$$

$$\tau=4.47\times10^{-12}m_{L^0}^{-5.19}U^{-2}\ \text{for}\ \nu_\mu\ \text{coupling}\,. \tag{5.20}$$

The fractional powers of m_{L^0} arise from a fit to the number of open decay channels as described in Ref. 58.

As the mixing parameter U^2 increases from 0, more heavy leptons would be produced in the dump. At the threshold value of U^2 enough decays would be observed in our detector to constitute a signal. As U^2 continues to increase, even more L^0 would be created, but because the lifetime decreases it becomes more probable that they decay before reaching the detector. As U^2 continues to increase the detector becomes insensitive. As shown in Fig. 23 for both $L^0\to e^+e^-\nu_e$ and $L^0\to\mu^+\mu^-\nu_\mu$ our data exclude an L^0 with mass between 10 and 600 MeV which couples with unit strength to ν_e or ν_μ.

A review of the experimental search for L^0 is given by Gilman and Rhie.[59] Generally, in the large-U^2 limit sensitivity is improved as the distance from target to detector decreases. In the small U^2 limit sensitivity is improved as beam flux increases. Results from the CHARM detector with a wideband beam[60] and for a beam-dump search[61] for $L^0\to e^+e^-\nu_e$ are also shown in Fig. 23. The distance to the CHARM detector is reflected in the less sensitive limits obtainable for large U^2 whereas the larger flux available to CHARM provides a more sensitive result at small U^2.

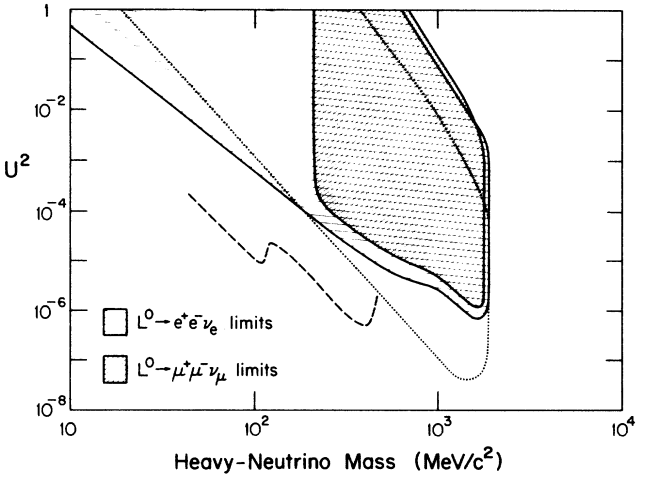

FIG. 23. Limits on the mixing angle U^2 as a function of the L^0 mass obtained from this experiment. One crosshatched area shows the exclusion for $L^0\to e^+e^-\nu_e$ at the 90% C.L.; the other shows the comparable $L^0\to\mu^+\mu^-\nu_\mu$ exclusion. The CHARM limits on U^2 for $L^0\to e^+e^-\nu_e$ obtained using a wide-band beam (Ref. 60) are shown as a dashed line and those obtained in a beam-dump search (Ref. 61) are shown dotted.

ACKNOWLEDGMENTS

We wish to acknowledge the invaluable services of the Fermilab staff and, in particular, the outstanding support of the Meson Laboratory personnel. We are indebted to a number of people for assistance during the setup and running of the experiment including J. Fitch, M. Jaworski, K. Mattison, J. Pluta, C. Ricci, C. Rush, and H. Schick. This work was supported in part by the U.S. Department of Energy under Contracts Nos. DE-AC02-76ER0081 (Wisconsin) and EY-76C-02-1545 (Ohio State), and by the National Science Foundation.

APPENDIX: MEASUREMENT OF TARGET-LENGTH EFFECTS

The measurement of the effect of the finite length of the targets by the detection of the neutrino flux would require a disproportionate fraction of beam time to achieve the necessary statistical accuracy. By measuring the nonprompt *muons* produced by decay in the target, however, data can be accumulated in several hours of operation per target sufficient to check the accuracy of the calculations.

This investigation used primarily the two partial-density copper targets, although data were also taken using other targets. The dimensions are as given in Table I; the shorter target is $2.79\lambda_{\text{abs}}$ in length; the longer $5.74\lambda_{\text{abs}}$. Calculations indicate that no correction is necessary for the long target and that the nonprompt muon flux obtained using the short target target should decrease by 16%.

The active shield (Fig. 8) was demagnetized, and the proton beam flux was reduced to ~10^8 per spill and measured using an ionization chamber. Muons of momentum less than ~31 GeV did not penetrate the iron shield and thus were not counted in the scintillation counter before the calorimeter. The momentum of muons which did penetrate the shield, the calorimeter, and at least two of the spectrometer toroids was measured. The coincidence of the scintillation counters in front of the calorimeter and the CC2 counter at the end of the spectrometer (Fig. 9) triggered the data acquisition. The resulting momentum distribution was described by an exponential function.

$$\frac{dN}{dp} = N_0 e^{-kp} , \quad k = 0.037 \pm 0.001 \qquad \text{(A1)}$$

with p in GeV/c.

The muon rates (i.e., the number of muons incident on the calorimeter per proton on target) measured for the long and the short partial-density Cu targets were nearly identical. However, several corrections must be applied to these raw rates: (1) The contribution to the rate due to beam interactions on material upstream of the target was removed (about 0.5%). (2) Muons will lose less energy in the shorter target resulting in a slightly lower-energy threshold with a consequent greater flux. The fractional change in rate due to this energy loss was calculated using the momentum spectrum

$$\frac{\Delta N}{N} = \frac{1}{N}\left[\frac{dN}{dp}\right]\left[\frac{dp}{dx}\right]\Delta x = k\left[\frac{dp}{dx}\right]\Delta x .$$

This results in a $\sim 3\%$ reduction of the rates for partial tungsten and the short partial Cu target. The correction to the rates for the other Cu targets was $\leq 1\%$. (3) Because of the hole on beam centerline (400 mm in diameter) for 10 m of the passive shield (Fig. 8), the acceptance increases (decreases) as the source is moved downstream (upstream). The rates were corrected to a standard distance (18.5 m) from the source to the center of the hole in passive shield. The corrected rate for the long partial Cu target is $\sim 7\%$ larger and that for the short target $\sim 4\%$ smaller. The corrections to the full density targets were $\leq 2\%$.

The measured rates for the full- and partial-density targets corrected as noted above are shown in Fig. 24. The measured rate for the short partial-density target corresponds to an effective density of 1.97 compared to the calculated value 2.01 ± 0.05. In Fig. 24 the rate is plotted at the calculated value of the effective density and lies within one standard error of the value interpolated using the long target ($\chi^2 = 0.6$ for 1 DF).

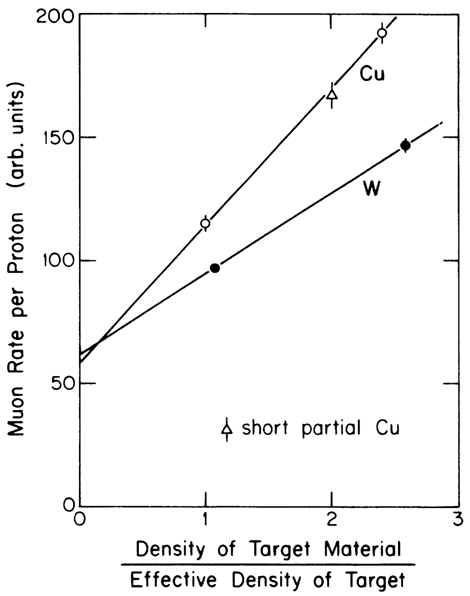

FIG. 24. The muon rate as measured in the scintillation counters at the calorimeter plotted as a function of the reciprocal effective density (normalized to the nominal density). The solid lines are determined by the rates using full-density and partial-density targets (long partial density for Cu). The rate for the short partial-density Cu target is plotted at the calculated value of effective density. The agreement of the Cu slope and short partial Cu rate corroborates the calculation of the short partial Cu effective density.

Further corroboration is found in the agreement of the ratio of slopes $R = a(\text{W})/a(\text{Cu})$ for muons as measured ($R_\mu = 0.44 \pm 0.08$) and calculated ($R_\mu = 0.61 \pm 0.12$). This comparison tests the A dependence of the background calculation as well as geometric effects. The same comparison can be made for the ν event rates (measured $R_\nu = 0.66 \pm 0.15$) and (calculated $R_\nu = 0.62 \pm 0.03$). In conclusion the assignment of the systematic errors for calculation of the background and effective densities is experimentally verified.

(a)Present address: General Electric Lighting Systems, Cleveland, OH 44112.

(b)Present address: Physics Department, University of Rochester, Rochester, NY 14627.

(c)Present address: Physics Department, Ohio State University, Columbus, OH 43210.

(d)Present address: Physics Department, Northwestern University, Evanston, IL 60201.

(e)Present address: Physics Department, Northeastern University, Boston, MA 02115.

(f)Present address: Bell Laboratory, Naperville, IL 60510.

(g)Present address: Physics Department, University of California at Berkeley, Berkeley, CA 94720.

(h)Present address: Fermilab, Batavia, IL 60510.

(i)Present address: Physics Department, Brown University, Providence, RI 02912.

(j)Present address: MS219, Fermilab, Batavia, IL 60510.

[1] A. C. Benvenuti *et al.*, Phys. Rev. Lett. **34**, 419 (1975).

[2] P. J. Wanderer, Jr., *et al.*, Phys. Rev. Lett. **23**, 729 (1969).

[3] J. J. Aubert *et al.*, Phys. Rev. Lett. **33**, 1404 (1974).

[4] J. E. Augustin *et al.*, Phys. Rev. Lett. **33**, 1406 (1974).

[5] G. Goldhaber *et al.*, Phys. Rev. Lett. **37**, 255 (1976).

[6] H. Abramowicz *et al.*, Z. Phys. C **13**, 179 (1982).

[7] M. Jonker *et al.*, Phys. Lett. **96B**, 435 (1980).

[8] P. Fritze *et al.*, Phys. Lett. **96B**, 427 (1980).

[9] E. L. Berger *et al.*, Phys. Rev. D **27**, 1080 (1983).

[10] For a recent comprehensive review of hadronic charm production, see A. Kernan and G. Van Dalen, Phys. Rep. **106**, 297 (1984).

[11] H. Wachsmuth, *Neutrino Mass and Low-Energy Weak Interactions*, proceedings of the Telemark III Miniconference, Cable, Wisconsin, 1984, edited by V. Barger and D. Cline

(World Scientific, Singapore, 1985), p. 307.

[12] For a more complete description of the beam line and the monitoring see J. Volk, Ph.D. thesis, Ohio State University, 1983.

[13] H. W. Atherton *et al.*, CERN Report No. 80-07 (unpublished).

[14] R. Blair *et al.*, Nucl. Instrum. Methods **226**, 281 (1983).

[15] A. Barton *et al.*, Phys. Rev. D **26**, 1497 (1982).

[16] P. Skubic *et al.*, Phys. Rev. D **18**, 3115 (1978).

[17] S. H. Oh, Massachusetts Institute of Technology APC Engineering Report No. 82-10 (unpublished).

[18] M. E. Duffy *et al.*, Nucl. Instrum. Methods **228**, 37 (1984).

[19] R. C. Ball *et al.*, Nucl. Instrum. Methods **197**, 371 (1982).

[20] J. Hoftun, Ph.D. thesis, Ohio State University, 1984.

[21] G. Conforto and T. Ricci (unpublished).

[22] M. Duffy, Ph.D. thesis, University of Wisconsin, 1983.

[23] E. Smith, Ph.D. thesis, University of Wisconsin, 1983.

[24] K. Barnham and N. Craigie, Nucl. Phys. **B154**, 463 (1979).

[25] H. Wachsmuth, CERN Report No. EP 79-125 (unpublished).

[26] M. E. Duffy *et al.*, Phys. Rev. Lett. **52**, 1865 (1984).

[27] O. Erriquez *et al.*, Phys. Lett. **80B**, 309 (1979).

[28] V. I. Efremenko *et al.*, Phys. Lett. **84B**, 511 (1979).

[29] J. Hanlon *et al.*, Phys. Rev. Lett. **45**, 1817 (1980).

[30] N. Armenise *et al.*, Phys. Lett. **102B**, 374 (1981).

[31] D. Allasia *et al.*, Phys. Lett. **107B**, 148 (1981).

[32] P. F. Jacques *et al.*, Phys. Rev. D **24**, 1067 (1981).

[33] N. J. Baker *et al.*, Phys. Rev. D **25**, 617 (1982).

[34] J. Marriner *et al.*, Phys. Rev. D **27**, 2569 (1983).

[35] R. Blair *et al.*, Phys. Rev. Lett. **51**, 343 (1983).

[36] R. C. Ball *et al.*, Phys. Rev. Lett. **51**, 743 (1983).

[37] F. Halzen, in *Proceedings of the XXI International Conference on High Energy Physics,* Paris, France, 1982, edited by P. Petiau and M. Proneuf [J. Phys. Paris Colloq., Suppl. 12, **43**, C3-381 (1982)].

[38] M. E. Duffy *et al.*, Phys. Rev. Lett. **55**, 1816 (1985).

[39] H. Cobbaert *et al.*, Phys. Lett. **191**, 456 (1987).

[40] C. Michael, in *Current-Hadron Interactions,* proceedings of the Fourteenth Rencontre de Moriond, Les Arcs, 1979, edited by J. Tran Than Van (Editions Frontieres, Dreux, France, 1979), Vol. 1.

[41] R. Ammar *et al.*, Phys. Lett. B **183**, 110 (1987).

[42] This branching ratio comes from the measured D^+ and D^0 semileptonic branching ratios of R. M. Baltrusaitis *et al.*, Phys. Rev. Lett. **54**, 1976 (1985), folded with the expected fraction of charged D mesons: $\rho = D^{\pm}/D_{\text{all}} = 0.27$.

[43] R. H. Schindler *et al.*, Phys. Rev. D **24**, 78 (1981).

[44] For a comparison see M. E. Duffy *et al.*, Phys. Rev. Lett. **57**, 1522 (1986).

[45] K. L. Giboni *et al.*, Phys. Lett. **85B**, 437 (1979).

[46] W. Lockman *et al.*, Phys. Lett. **85B**, 443 (1979).

[47] D. Drijard *et al.*, Phys. Lett. **85B**, 452 (1979).

[48] A. Aleev *et al.*, Yad. Fiz. **35**, 1175 (1982) [Sov. J. Nucl. Phys. **35**, 687 (1982)].

[49] T. Aziz *et al.*, Nucl. Phys. **B199**, 424 (1982).

[50] S. F. Biagi *et al.*, Phys. Lett. **122B**, 455 (1983).

[51] J. F. Gunion, Phys. Lett. **88B**, 150 (1979).

[52] E. Vella *et al.*, Phys. Rev. Lett. **48**, 1515 (1982).

[53] J. Campbell *et al.*, Phys. Rev. Lett. **30**, 335 (1973).

[54] S. J. Barish *et al.*, Phys. Rev. Lett. **36**, 179 (1976).

[55] G. Fanourakis *et al.*, Phys. Rev. D **21**, 562 (1980).

[56] R. C. Ball *et al.*, Phys. Rev. Lett. **53**, 1314 (1984).

[57] See the recent review by B. A. Lyubimov, in *Proceedings of the XXII International Conference on High Energy Physics,* Leipzig, East Germany, 1984, edited by A. Meyer and E. Wieczorek (Akadamie der Wissenschaften der DDR, Zeuthen, 1984).

[58] M. Gronau, C. N. Leung, and J. Rosner, Phys. Rev. D **29**, 2539 (1984).

[59] F. Gilman and S. Rhie, Phys. Rev. D **32**, 324 (1985).

[60] F. Bergsma *et al.*, Phys. Lett. **128B**, 361 (1983).

[61] K. Winter, in *Proceedings of the 1983 International Symposium on Lepton and Photon Interactions at High Energies,* Ithaca, New York, edited by D. G. Cassel and D. Kreinick (Newman Laboratory of Nuclear Studies, Cornell University, Ithaca, 1983), p. 177.

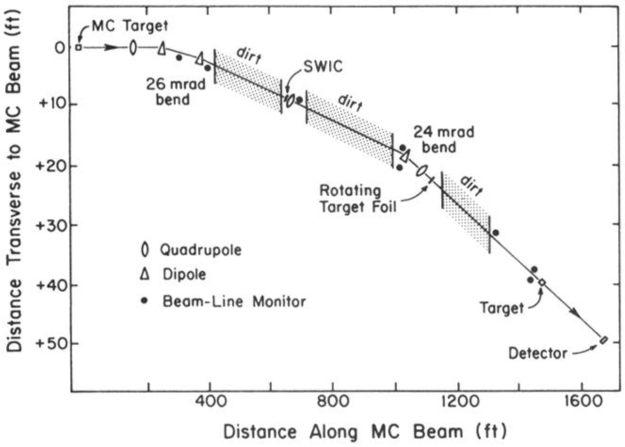

FIG. 1. Plan view of the $M2$ beam line upstream of the experiment showing the MC target, the two bends leading to the dump target, and the positions of the beam-line monitors, of the SWIC, and of the rotating foil used to measure the halo background.

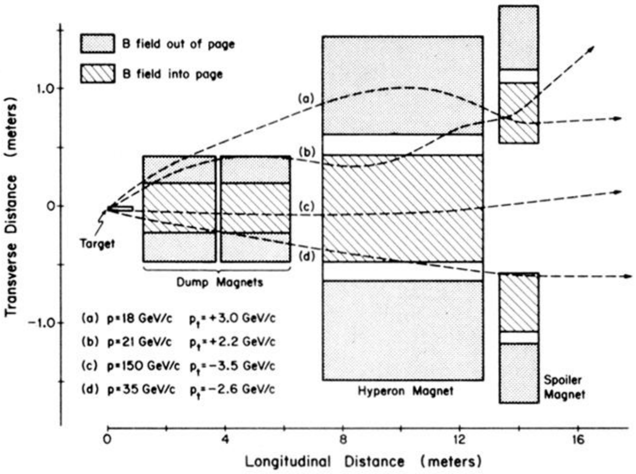

FIG. 7. A vertical section through the active muon shield showing the target-block assembly, the iron-core dump magnets, the hyperon magnet, and the spoiler magnets. Four μ^- trajectories (a)–(d) are shown which illustrate the complications resulting from the return-flux deflection. Only muon (d) intersects the detector.

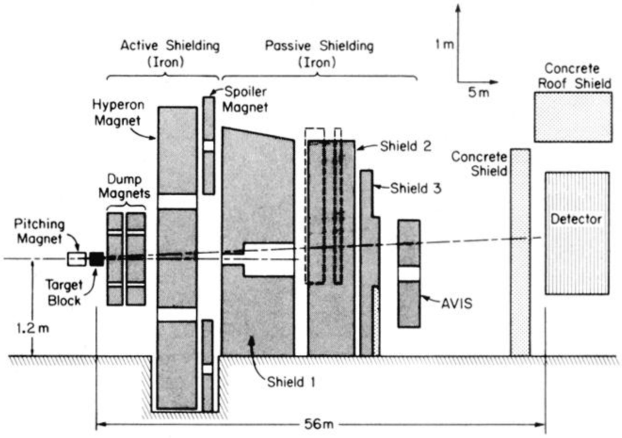

FIG. 8. A vertical section through the experiment showing the muon shielding, both active and passive, for run 2. For run 1, iron blocks, shown by the dotted lines, were used in place of shields 2 and 3. The gap in shield 1 was a 400-mm-diameter beam-pipe setup for a previous experiment.